Characteristics of the flow around finite wall-mounted square cylinders and the mechanism of tonal noise

Yanan Wang (王亚南),[1, 2, a)] Boyu Ma (马博域),[1, b)] Zhiwei Hu (胡志伟),[3, c)] and David Thompson[2, d)]

[1)] *School of Mechanical Engineering, Xi'an Jiaotong University, Xi'an 710049, PR China.*

[2)] *Institute of Sound and Vibration Research, University of Southampton, Southampton, SO17 1BJ, United Kingdom.*

[3)] *Department of Aeronautics and Astronautics, University of Southampton, Southampton, SO17 1BJ, United Kingdom.*

(Dated: 31 May 2024)

Motivated by the need to reduce the noise from train pantographs, numerical simulations are carried out for the flow over finite wall-mounted square cylinders with different aspect ratios at a Reynolds number of 1.5×10^4. Five aspect ratios (height-to-width ratios) are taken into account, namely, 1.4, 4.3, 7.1, 10 and 12.9. The effect of the aspect ratio on the aerodynamic coefficients, the near-wall flow topologies and the pressure distributions are studied in detail to give insight into the noise generation mechanisms. The pressure rate of change $\mathrm{d}p/\mathrm{d}t$ on the cylinder surfaces is adopted to evaluate the dipole noise source. It turns out that distributions of $\mathrm{d}p/\mathrm{d}t$ are closely related with flow evolutions near the free ends and the wall-mounting junctions of cylinders with different aspect ratios. High levels of $\mathrm{d}p/\mathrm{d}t$ are found close to lateral trailing edges of the cylinder, while the strength grows quickly as the aspect ratio is increased. The far-field noise emitted from these cylinders is predicted using the Ffowcs Williams–Hawkings acoustic analogy and validated with wind tunnel measurements available in the literature. For receivers located in the cross-flow direction, a single acoustic tone near a Strouhal number of 0.1 is observed for cylinders with aspect ratios not greater than 7, while an additional tone at a higher Strouhal number occurs as the aspect ratio is further increased. The underlying mechanism of the tonal noise emitted to the far field is also investigated by combining the noise source localization and dynamic mode decompositions.

Keywords: Aspect ratio; Finite wall-mounted cylinders; Flow topology; Aerodynamic noise

---

[a)] Electronic mail: yananwang@xjtu.edu.cn

[b)] Electronic mail: shaken960m@163.com

I. INTRODUCTION

The flow around finite wall-mounted cylinders (FWMCs) is a fundamental problem relevant to many industrial applications, such as aircraft landing gears, train pantographs and buildings. Moreover, studying the flow characteristics is also fundamental to understanding the underlying physics for the aerodynamic noise emitted. Pantographs, mounted on the train roof, consist mostly of cylinders with different lengths. Motivated by the need to reduce the aerodynamic noise from the pantographs, the flow dynamics and the sound induced by FWMCs with different aspect ratios are investigated numerically in this paper. The mechanism of tonal noise is also studied based on the dynamic mode decomposition (DMD).

The flow patterns surrounding FWMCs differ considerably from those surrounding cylinders with infinite length, due to the additional flow phenomena occurring near the free end, the wall junction and their interactions[1–5]. Porteous et al.[6] reviewed studies on the flow patterns in the wake of FWMCs and summarised several flow models to describe the flow structure near the tip and the wall-mounting junction of the cylinders. Yauwenas et al.[7] conducted both experimental and numerical investigations to characterise the near-wake flow topology of square FWMCs with aspect ratios (length/width) ranging from 1.4 to 21.4. The surface pressure and the near-wake velocity were measured in a wind tunnel at Reynolds numbers (Re) of 1.1×10^4 and 1.4×10^4. To obtain more flow details, large eddy simulations (LES) were also performed for four representative aspect ratios, 1.4, 4.3, 10 and 18.6. The near-wake flow patterns were visualised using a vortex core detection method and a parametric diagram was proposed to categorize the four shedding regimes that were identified in the wake. Cao et al.[8] provided topological descriptions on the near-wall flow around a square FWMC at a Reynolds number of 5×10^4 and the aspect ratio of the cylinder was 3. High-resolution simulations and critical-point theory were used to construct flow topologies from the bottom to the top. It was found that the trailing-edge vortices, discovered only at a high Reynolds number, cause a sharp drop in pressure near the trailing edge.

Flow developments around the FWMCs are also affected by the incoming flow. The influence of the incoming boundary layer thickness on the flow dynamics of square FWMCs at $Re = 1.4 \times 10^4$ was investigated numerically

---

[c] Electronic mail: z.hu@soton.ac.uk

[d] Electronic mail: djt@isvr.soton.ac.uk

by Chen et al.[9]. Six different boundary layer thicknesses (expressed as δ/D, where D is the cylinder width) ranging from 0.5 to 4 were considered for cylinders with aspect ratios of 6 and 10. In their work, flow characteristics including the aerodynamic force, surface pressure and turbulence intensity were discussed and the dependence of the wake structures on both the boundary layer thickness and the aspect ratio was analysed. Behera and Saha[10] conducted direct numerical simulations (DNS) on the flow over a square FWMC with an aspect ratio of 7 at a Reynolds number of 250. The thickness of the incoming boundary layer was varied from 0 to 0.3 times the cylinder height. Two shedding modes were observed in the wake of the cylinder for all the considered boundary layer thicknesses. In addition, the overall drag coefficient was found to decrease as the wall boundary layer thickness increased. Shinde et al.[11] explored the effect of the incoming boundary layer thickness on the vortical structures in the wake of a wall-mounted cube (a square cylinder with an aspect ratio of 1). The cube was placed in a spatially evolving turbulent boundary layer and the flow features were obtained using wall-resolved LES. It was found that the strength of the horseshoe vortex scaled with the cube size and the decay of the near-wake turbulent kinetic energy (TKE) followed a power law.

Instead of the height-to-length ratio, Rastan et al.[12] investigated the influence of the cross-sectional shape on the wake dynamics of a wall-mounted rectangular cylinder using LES at a Reynolds number of 1.2×10^4. The cross-sectional aspect ratio, namely the width (cross-flow direction) over the length (streamwise direction), of the cylinder ranged from 1 to 4, while the ratio of the height over the length was kept at 7. Two types of spiral vortices over the top surface were reported and analysed in detail. Conceptual models of the flow patterns in the wake were also proposed in their work.

Compared with the flow dynamics, the noise emitted from FWMCs has been studied less. Moreau and Doolan[13] measured the sound generated by FWMCs with both circular and square cross-sections in an anechoic wind tunnel. A wide range of aspect ratios from 0.29 to 22.9 were taken into account and the measurements were carried out at three flow speeds. Multiple peaks were observed in the noise spectra, which were related with different vortex cells in the near wake dependent on the aspect ratio. In addition, the number of dominant tones in the noise spectra changed with the aspect ratio. More detailed experiments at a Reynolds number of 1.4×10^4 on the square FWMCs with the same range of aspect ratios were conducted by Porteous et al.[14] to explore further the dependence of the aeroacoustics and the flow features on the aspect ratio. Four shedding regimes were classified and identified from the multiple tones found in the noise spectra. Conceptual sketches of the vortex structure in the near wake responsible for each tone were also given and discussed based on the velocity profiles measured by hot-wire anemometers. Both the noise and the flow field generated by a square FWMC with an aspect ratio of 6 were investigated experimentally by Becker et al.[15]. Fore- and aft- bodies were attached to the cylinder to investigate the effect of changes in the geometry. It was found that reducing the symmetry and stability of the vortex street while keeping a constant separation line showed promising results in suppressing the noise. Geyer[16] reported experimental research regarding the influence of porous covers on reducing the aerodynamic noise from a circular FWMC. The study showed that replacing the wall end of the cylinder with the porous material was more effective than applying it at the free end.

For the purpose of noise control, it is important to identify the underlying flow patterns closely correlated with the far-field noise. Since Schmid[17] originally introduced the DMD technique within the fluid dynamics community, it has provoked interests in extracting relevant dynamic modes from complicated flow. More recently, the DMD technique has also been applied in exploring the underlying mechanisms of the emitted aerodynamic noise. Burak et al.[18] employed DMD and shadowgraph imagery to study the screech noise emitted from a single expansion ramp nozzle. A low-frequency mode was captured by the DMD method, which is also observed in the near-field acoustic spectra. Prasad and Gaitonde[19] proposed a time-domain linear approach to predict jet noise and the DMD method was used to validate their algorithm. Broatch et al.[20] adopted the DMD to analyse the noise from Unmanned Aerial Vehicles. The propeller acoustic modes were extracted and shown in pairs describing a rotating flow structure. The combustion noise in a gas turbine engine was also studied by Broatch et al.[21], a precessing vortex core and a vortex breakdown bubble were confirmed using the DMD analysis. Yang et al.[22] located the noise source on a three-dimensional NACA66 hydrofoil surface by performing DMD on the surface pressure data. It was shown that the alternating regions of high and low amplitude in the mode exhibit a high degree of overlap with the regions of cavitation transition.

As reviewed above, although the flow characteristics and aerodynamic noise from FWMCs are of great interest due to their wide applications in industry, most of the existing research focuses on flow patterns in the wake. However, the near-wall flow and the noise emitted to the far field have not been studied to the same extent. The near-wall flow topologies are critical for a better understanding of the fluctuating pressure acting on the cylinder surfaces. The underlying flow patterns related with the far-field noise also need to be analysed. In the current work, flow features including the near-wall flow topologies for square FWMCs with five different aspect ratios are examined in detail at a Reynolds number of 1.5×10^4 (based on the width of the cylinder), which lies in the range where the flow over a square cylinder is independent of Reynolds number[23]. The flow is solved numerically using the delayed detached eddy simulation (DDES) in the open-source software OpenFOAM (version 2.4.0). Based on the flow simulations, the fluctuating pressure acting on the cylinder surfaces is sampled. The far-field noise is then predicted and analysed using the Ffowcs Williams–Hawkings (FW–H) acoustic analogy. In addition, the mechanism of the tonal noise emitted to the far field is also investigated and discussed by combining noise source localization and the DMD technique.

II. NUMERICAL METHOD

A. Governing equations

Conventionally, the flow can be assumed to be incompressible at low Mach numbers for most purposes. This assumption is generally considered to be reasonable for Mach numbers up to 0.3.[24] As the flow speed used in this work is 32 m/s, corresponding to a Mach number of about 0.1, the flow simulations are based on solving the incompressible Navier-Stokes (N-S) equations. To balance the computational cost and the numerical accuracy, the hybrid DDES turbulence model is adopted for the computational fluid dynamics (CFD) simulations. DDES is designed to solve the boundary layer using the Reynolds-averaged Navier–Stokes (RANS) method and to use the LES mode elsewhere[25,26]. In this way, the grid resolution close to the solid walls could be much less demanding than that required by LES, where cubic grids are preferred, even in the boundary layer region[27]. Therefore, this hybrid model is particularly practical to solve the flow with massive separations at high Reynolds numbers. The one-equation Spalart–Allmaras (S–A) turbulence model is adopted to solve the boundary layer region[25]. This has been developed for separated boundary layer flow and is able to reproduce the viscous sublayer near the solid walls[28]. DDES is proposed to ensure the transition process from the RANS mode to the LES mode happens outside the boundary layer and to overcome some inherent deficiencies that may occur with the traditional Detached Eddy Simulation (DES), such as modelled stress depletion[29] and grid induced separation[30]. More explanations can be found in Ref. [31].

B. Ffowcs Williams-Hawkings acoustic analogy

In principle, the far-field aerodynamic noise can be captured by solving the unsteady compressible N-S equations directly. However, it is hard to achieve in practice, considering the demanding computational cost. Therefore, a hybrid approach is adopted in the present work, that involves calculating the surface pressure in CFD and using it to predict the sound propagation using the FW-H acoustic analogy. The FW-H equation is derived from the compressible N-S equations taking into account moving boundaries in the flow[32]. The wave operator is arranged on the left-hand side of the FW-H equation while the equivalent noise sources are put on the right-hand side as follows:

$$\frac{1}{c_0^2}\frac{\partial^2[p'H(f)]}{\partial t^2} - \nabla^2[p'H(f)] = \frac{\partial^2}{\partial x_i \partial x_j}[H(f)T_{ij}] - \frac{\partial}{\partial x_i}[\delta(f)F_i] + \frac{\partial}{\partial t}[\delta(f)Q] \qquad (1)$$

where c_0 is the sound speed of undisturbed medium in the far field and p' is the fluctuating pressure. T_{ij}, F_i and Q represent the equivalent quadrupole, dipole and monopole sources, respectively. $H(f)$ is the Heaviside function and $\delta(f)$ is the Dirac delta function, which are used to indicate the position of the surfaces according to the variable f. More details can be found in Ref. [32]. Since the noise at lower values of the Strouhal number (St) is of more interest in this work, the FWMCs are assumed to be acoustically compact, which is more computationally economical in far-field noise prediction. Although the ground is also a legitimate part of the boundary, only the noise emitted from the cylinders is studied. In addition, to validate the predicted noise with the measurements reported by Porteous et al.[14], the noise reflected from the ground is not included, to be consistent with the experiments. Details of the experimental setup can be found in the Reference [14]. As discussed above, the free-space Green's function is adopted in this work to predict the far-field noise. The solution of the FW-H equation based on the free-space Green's function[33] can be written as:

$$\begin{aligned} p'(\mathbf{x},t) =& \frac{\partial^2}{\partial x_i \partial x_j} \int_V \frac{T_{ij}(\mathbf{y}, t - |\mathbf{x}-\mathbf{y}|/c_0)}{4\pi|\mathbf{x}-\mathbf{y}|} \mathrm{d}\mathbf{y} \quad - \frac{\partial}{\partial x_i} \int_S \frac{F_i(\mathbf{y}, t - |\mathbf{x}-\mathbf{y}|/c_0)}{4\pi|\mathbf{x}-\mathbf{y}|} \mathrm{d}\mathbf{y} \\ &+ \frac{\partial}{\partial t} \int_S \frac{Q(\mathbf{y}, t - |\mathbf{x}-\mathbf{y}|/c_0)}{4\pi|\mathbf{x}-\mathbf{y}|} \mathrm{d}\mathbf{y} \end{aligned} \tag{2}$$

where $p'(\mathbf{x}, t)$ is the sound pressure at the position $\mathbf{x}$ induced by the sound sources at the position $\mathbf{y}$. V and S denote the control volume and the control surface of the FW-H acoustic analogy, respectively.

In this work, the cylinder surfaces are chosen as the FW-H integration surface and the fluctuating pressures sampled from these surfaces based on CFD are adopted as the dipole sources. Although the above FW-H equation is derived from full compressible N-S equations, in which both hydrodynamic and acoustic pressures contribute to the dipole source, the incompressible flow simulation cannot resolve the acoustic part. Nevertheless, in the near field, especially on the cylinder surfaces, the hydrodynamic pressure is utterly dominant[34] and the far-field noise can be adequately predicted from the incompressible flow simulation, provided that there is no acoustic feedback affecting the flow. Since the FWMCs are treated as rigid bodies, no pulsating monopole sources exist. Moreover, as the Mach number studied in this work is smaller than 0.1, quadrupole sources in the turbulent flow can be neglected[35]. Therefore, only the second term on the right-hand side of Eq. 2 is retained, and in the acoustic far field the spatial derivative in this term can be converted to a time derivative, namely,

$$p'(\mathbf{x},t) = \frac{\partial}{\partial t} \int_S \frac{p_i(\mathbf{y}, t - |\mathbf{x}-\mathbf{y}|/c_0)}{4\pi c_0 |\mathbf{x}-\mathbf{y}|} \mathrm{d}\mathbf{y} \tag{3}$$

As implied by Eq. 3, the sound pressure in the far field emitted from a single dipole source is proportional to the pressure fluctuation rate $\mathrm{d}p/\mathrm{d}t$ on the solid surfaces:

$$p'(\mathbf{x},t) \propto \frac{\mathrm{d}p(\mathbf{y},t-|\mathbf{x}-\mathbf{y}|/c_0)}{\mathrm{d}t} \tag{4}$$

Therefore, Eq. 4 can be used to assess the dipole source propagating to the far field. In order to examine the distribution of the dipole source strength on the cylinder surfaces, the following equation is applied:

$$L_{\dot{p}} = 10\log_{10}\left(\sum_{i=1}^{n}\mathrm{PSD}_i \times \Delta f\right) \tag{5}$$

where PSD_i indicates the power spectral density of the $\mathrm{d}p/\mathrm{d}t$ signal at the i^{th} frequency, Δf is the frequency resolution and n is the total number of frequencies included in the sum.

C. Dynamic mode decomposition

The physical flow features related with certain frequencies can be extracted using the DMD, with each mode representing the spatial structures of the flow oscillating at a single characteristic frequency[36]. Therefore, studies on the underlying mechanisms in aeroacoustics can benefit greatly from this approach, especially for tonal noise with predominant frequencies. The DMD is purely a data-driven technique, which combines benefits of proper orthogonal decomposition (POD) and the discrete Fourier transform[37,38]. The inputs of the DMD are snapshots from fluid measurements or simulations, which are normally time series of fluctuating variables with a constant time interval. For example, a snapshot sequence $\mathbf{V}_1^N$ is given as a matrix:

$$\mathbf{V}_1^N = \{v(t_1), v(t_2), v(t_3), ..., v(t_n)\} \tag{6}$$

where $v(t_i)$ stands for the ith flow field sample. Similarly, the matrix $\mathbf{V}_2^{N+1}$ can be arranged as:

$$\mathbf{V}_2^{N+1} = \{v(t_2), v(t_3), v(t_4), ..., v(t_{n+1})\} \tag{7}$$

When the time interval Δt between two consecutive snapshots is small enough, the snapshots can be assumed to satisfy a linear relationship, namely,

$$v(t_{i+1}) = \mathbf{A}v(t_i) \tag{8}$$

and

$$\mathbf{V}_2^{N+1} = \mathbf{A}\mathbf{V}_1^N \tag{9}$$

where the matrix $\mathbf{A}$ is the linear mapping. Based on the eigenvalues λ_i and the corresponding DMD modes ϕ_i of the matrix $\mathbf{A}$, the relevant flow modes can be extracted. Since the DMD is based on linear algebra, different algorithms and interpretations have been developed[39–41]. In this paper, the classic least squares method is adopted to compute the matrix $\mathbf{A}$. The time interval Δt is chosen as 1×10^{-4} s and 4000 snapshots are used for each DMD analysis.

III. COMPUTATIONAL SETUP

A sketch of the computational domain is shown in Fig. 1. The origin of the coordinate system is located on the ground at the bottom centre of the cylinder. The length, height and width of the square FWMC are represented by L, H and W along the streamwise (x), the spanwise (y) and the cross-flow (z) directions. Since square cylinders are considered in this work, the length and width are equal ($L = W$). The width of the cylinder is W =7 mm and is kept constant, and the aspect ratio is defined as the height divided by the width, namely, $AR = H/W$. Five aspect ratios are studied, 1.4, 4.3, 7.1, 10 and 12.9. The velocity of the incoming flow is $U_\infty = 32$ m/s, corresponding to a Reynolds number of 1.5×10^4 based on the width W of the cylinder. As depicted in Fig. 1, the overall size of the computational domain is $31L \times 5H \times 21W$, with $10L$ upstream of the cylinder and $20L$ downstream. The size in the spanwise direction varies depending on the cylinder aspect ratio. The assigned boundary conditions are also shown in Fig. 1.

The computational domain is discretized using fully-structured grids. The height of the first layer cells (Δ_{y1}) normal to the cylinder surfaces is calculated to target the non-dimensional first cell height at the wall (y_1^+) to be 1.5. The size of the first layer grids along the streamwise direction is the same as that in the cross-flow direction, and is denoted as $\Delta_{x1,z1}$. The minimum value of $\Delta_{x1,z1}$, namely, $\min(\Delta_{x1,z1})$ can be found at the sharp corners of the cylinders, while the maximum, $\max(\Delta_{x1,z1})$ is in the middle of the longest sides. The grid sizes are coarsened progressively with a stretching ratio of 1.09, with the finest grids close to the cylinder surfaces. Details of the grids are summarised in Table I, where N_{grid} means the total number of cells. The mesh resolution is decided based on both the benchmark case on a wall-mounted cube, which has been evaluated carefully in the previous work[42], and the grid independence investigations conducted on cylinders with different aspect ratios in cross flow in Ref. [43]. Fig. 2

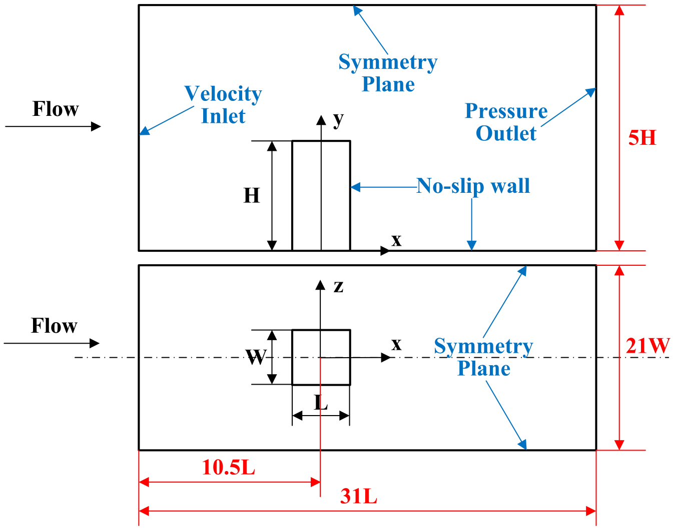

FIG. 1. Sketch and boundary conditions of the computational domain

shows distributions of y_1^+, which is more related with the noise prediction, along the cylinder surfaces and also the ground on the $z = 0$ plane for the case with $AR = 1.4$ by way of example. As can be seen, most of the y_1^+ values are smaller than 1, while the maximum is less than 2. The time step of these simulations is set as 1×10^{-6} s to ensure the Courant–Friedrichs–Lewy (CFL) numbers are smaller than 2.

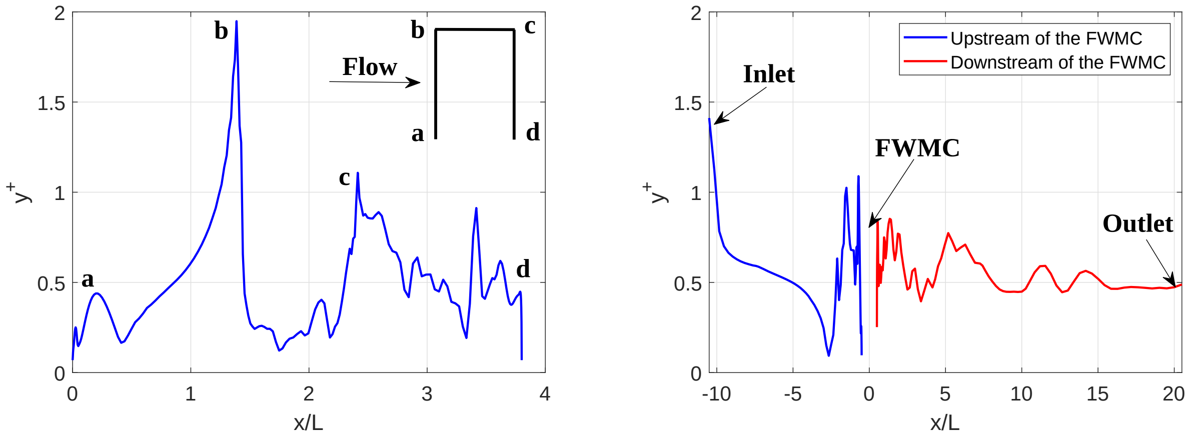

(a) y_1^+ around the FWMC

(b) y_1^+ along the ground

FIG. 2. The distribution of y_1^+ along the solid walls in the $z = 0$ plane for the case $AR = 1.4$.

Additional grid dependence investigations are also carried out on the bounding cases with $AR = 1.4$ and 12.9 to gain further confidence on the meshing strategy described above. The adopted mesh resolutions are either coarsened or refined by a ratio of $\sqrt{2}$ for trial. Mean and root mean square (rms) values of aerodynamic coefficients $C_a = F_a/(0.5\rho U_\infty^2 A)$ for $AR = 1.4$ and 12.9 corresponding to different meshes are summarised in Table II, where F_a is

AR	Δ_{y1}/W	$\min(\Delta_{x1,z1})/W$	$\max(\Delta_{x1,z1})/W$	N_{grid}
1.4	1.7×10^{-3}	1.29×10^{-2}	3.29×10^{-2}	1.69×10^{6}
4.3	1.7×10^{-3}	1.29×10^{-2}	10.1×10^{-2}	2.57×10^{6}
7.1	1.7×10^{-3}	1.29×10^{-2}	11.5×10^{-2}	3.03×10^{6}
10	1.7×10^{-3}	1.29×10^{-2}	12.8×10^{-2}	3.10×10^{6}
12.9	1.7×10^{-3}	1.29×10^{-2}	14.2×10^{-2}	3.66×10^{6}

TABLE I. Details of the structured grids for the FWMCs

the drag (along the x direction), lift (along the y direction) or side force (along the z direction) for C_d, C_l or C_s, respectively and the frontal area is chosen as the reference area, namely $A = H \times W$. These aerodynamic coefficients are sampled from a normalised time $t^* = tU_\infty/W = 500$ to 2000. Due to the symmetry of the geometry, the mean side force coefficient $\overline{C_s}$ is close to zero and is not listed in Table II. As indicated by the grid dependence studies, statistical convergence has been achieved, since both mean and rms values of these coefficients only change slightly when the adopted mesh is further refined.

AR	mesh	N_{grid}	$\overline{C_d}$	$\overline{C_l}$	$C_{\text{d},rms}$	$C_{\text{l},rms}$	$C_{\text{s},rms}$
1.4	coarse	0.93×10^{6}	1.345	0.484	0.0431	0.0434	0.1602
1.4	adopted	1.69×10^{6}	1.269	0.448	0.0359	0.0374	0.1393
1.4	refined	2.50×10^{6}	1.268	0.445	0.0352	0.0369	0.1368
12.9	coarse	2.00×10^{6}	1.930	0.118	0.1195	0.0052	0.4797
12.9	adopted	3.66×10^{6}	1.874	0.111	0.1013	0.0043	0.4100
12.9	refined	5.75×10^{6}	1.880	0.109	0.1014	0.0041	0.4220

TABLE II. Grid dependence investigations on the cylinders with $AR = 1.4$ and 12.9.

IV. VALIDATION OF THE NUMERICAL METHODS

The numerical method described in Section II has been validated extensively and reported in our previous work[42–44]. Firstly, the measurements conducted by Castro and Robins[45] on the flow over a wall-mounted cube at a Reynolds number of 5×10^4 were re-implemented numerically using DDES. Good agreement was achieved between the experimental and the numerical results, including the velocity profiles and the turbulence intensity at different positions in the wake, together with the distributions of the pressure coefficient along the cube surfaces. Details can be found in

Ref. [42]. In addition, the use of DDES to predict the near-wall flow topologies was also validated by comparisons with the near-wall Particle Image Velocimetry measurements on a wall-mounted cube conducted by Depardon et al.[46]. Another benchmark case on the flow over a sphere at a Reynolds number of 5×10^4 was also implemented by the authors[44] to increase confidence in the adopted numerical methodologies, especially in predicting the location of the flow separation. Apart from the velocity and the pressure, the skin friction coefficient C_f around the sphere obtained from the simulation also agreed well with the measurements in the literature[47]. Particularly, the location of flow separation indicated by $C_f = 0$ was captured accurately. The effect of aspect ratio on the flow over square cylinders in cross flow was also studied in our previous work[43], where thorough grid dependence investigations were carried out on the cylinders with aspect ratios of 1/6 and 12. The computational domain described in Section III was discretized based on criteria of the most suitable mesh resolution derived from the above benchmark cases and grid dependence studies.

Apart from these previous studies, the mean streamwise velocity and the root mean square (rms) values of the streamwise velocity for FWMCs with aspect ratios of 1.4, 4.3 and 10 obtained from the present work are compared with those reported by Yauwenas et al.[7] as shown in Fig. 3. The red lines in Fig. 3 denote the current results of this work, while the black lines with squares are the data measured in a wind tunnel and the blue lines are obtained using LES by Yauwenas et al. As can be seen, the velocity profiles derived from the present work agree reasonably well with the data in the literature. In addition, comparisons between the predicted noise spectra (power spectral density, PSD) in the present work and the measurements presented by Porteous et al.[14] for FWMCs with aspect ratios of 4.3 and 12.9 are depicted in Fig. 4. The agreement in Fig. 4 confirms the validity of the proposed method.

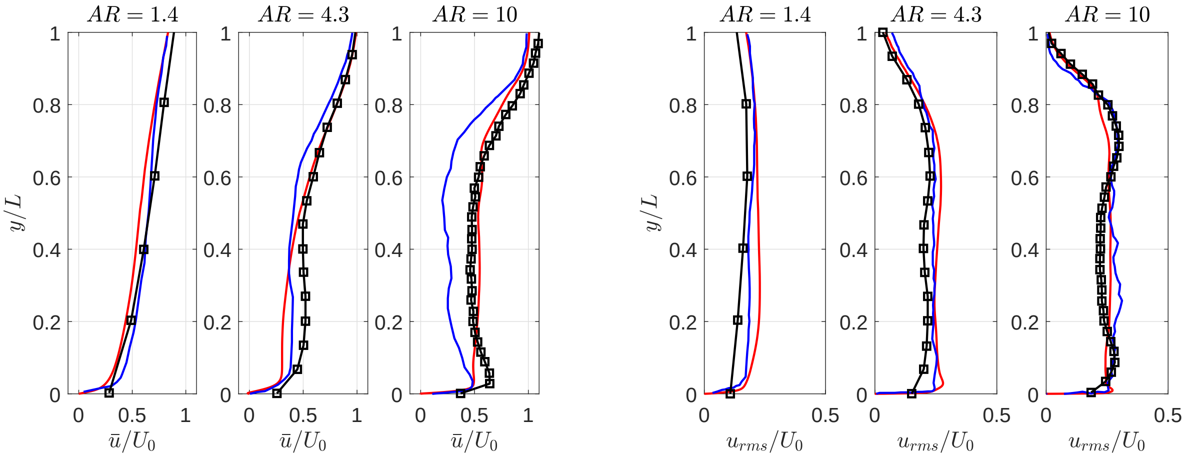

(a) Comparisions velocity

(b) Comparisions velocity rms

FIG. 3. Comparisons of the velocity profiles at $x/W = 4$ on the plane $y/W = 0.6$ obtained from the present work and the results reported by Yauwenas et al.[7] —: Present work; —: LES, Yauwenas; —□— : experiments, Yauwenas.

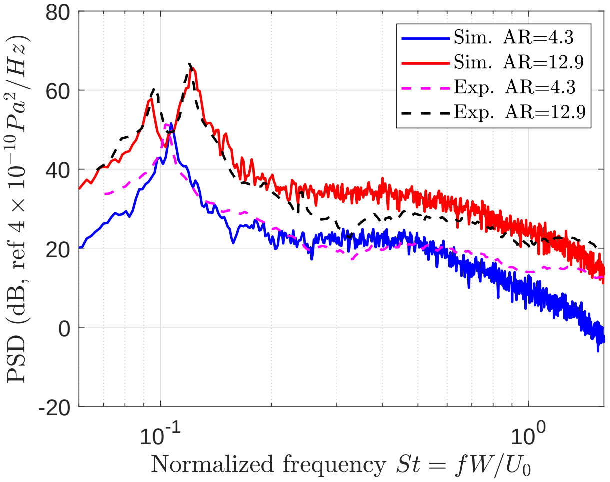

FIG. 4. Comparisons of the noise spectra predicted by the present work and the measurements conducted by Porteous et al.[14]

V. EFFECT OF THE ASPECT RATIO ON THE FLOW

A. Aerodynamic coefficients

Fig. 5 summarises mean and rms values of aerodynamic coefficients for the square FWMCs with different aspect ratios. Definitions of these parameters are given in Sec. III, and the frontal area $H \times W$ is chosen as the reference area. The mean aerodynamic coefficients change progressively with the increase of the aspect ratio. The mean side force coefficients ($\overline{C_s}$) are always close to zero, indicating convergence of the statistics for these symmetric geometries; however, the mean drag coefficient ($\overline{C_d}$) increases considerably with increasing aspect ratio while the mean lift coefficient $\overline{C_l}$ reduces gradually. Fluctuations of these force coefficients can be seen in the rms values in Fig. 5(b). $C_{\mathrm{s},rms}$ for the side force coefficients has the largest values and is most affected by the aspect ratio.

PSDs of C_d, C_l and C_s are displayed in Fig. 6. For the purpose of smoothing, these spectra are calculated using Welch's method with a Hanning window, which is conventionally used due to the reduced spectral leakage. The width of the window is about 0.26 s and ten segments are used with 50% overlap. The frequency resolution is about 3.8 Hz, corresponding to a Strouhal number of 8.3×10^{-4}. Distinct peaks can be found in the spectra of C_d and C_s in Fig. 6(a) and 6(c), while only small peaks are found for the cylinders with $AR = 10$ and 12.9 in C_l in Fig. 6(b). In particular, these peaks tend to be very sensitive to the changes in aspect ratio in terms of both the number of peaks and the range of frequencies, as displayed in the zoomed subfigures, indicating the presence of different flow regimes depending on the aspect ratio. Details of the flow patterns for these cylinders will be discussed in the following section.

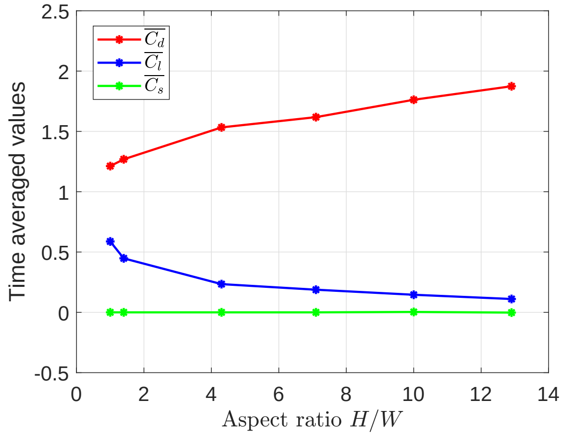

(a) The mean aerodynamic coefficients (b) The rms values of the aerodynamic coefficients

FIG. 5. Mean and rms values of C_d, C_l and C_s for cylinders with different aspect ratios.

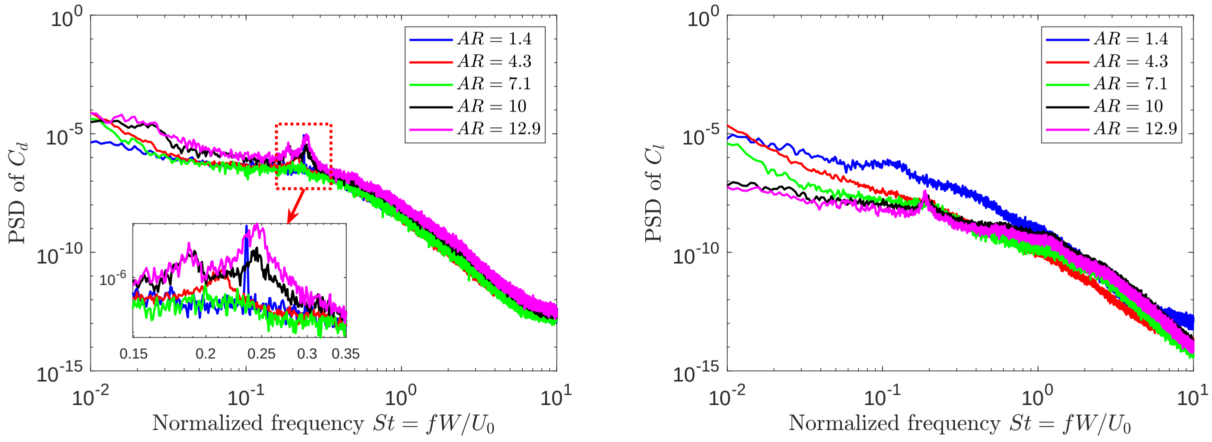

(a) C_d (b) C_l

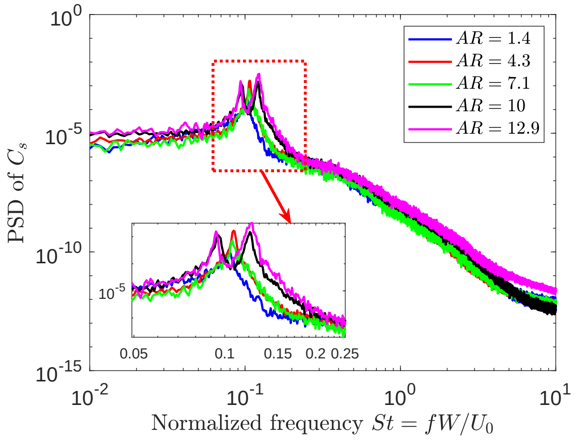

(c) C_s

FIG. 6. PSDs of C_d, C_l, C_s for cylinders with different aspect ratios.

B. Flow patterns around the cylinders

Three-dimensional flow structures around the square FWMCs with different aspect ratios are visualised in Fig. 7, which shows the instantaneous flow structures based on the iso-surface of the Q-criterion[48], at a normalised value $Q_n = Q/(U_\infty/W)^2 = 0.1$ and coloured by the mean streamwise velocity. The flow patterns around the cylinders are affected noticeably as the aspect ratio increases. The flow pattern for $AR = 10$ (not shown) is similar to that for $AR = 12.9$. Horseshoe vortices can be observed along the ground, running from upstream to the sides of these cylinders, but they tend to be more evident with a smaller aspect ratio. In addition, abundant vortices of different scales are formed in the wake of the cylinders. As expected, the flow structure along the spanwise direction becomes more and more coherent with the increase of the aspect ratio. This occurs because the flow near the mid-span is less affected by the downwash flow from the top of the cylinders and the horseshoe vortices around the wall-mounting junction, which allows the development of the vortex shedding along the spanwise direction.

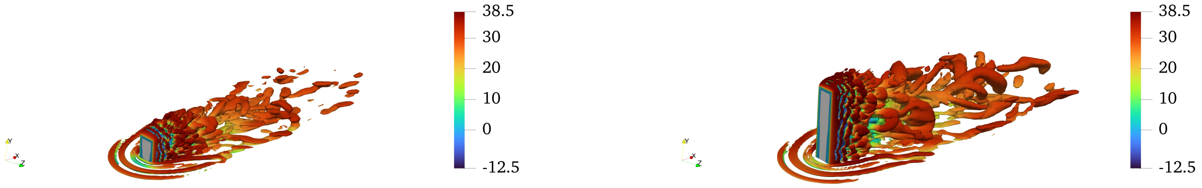

(a) $AR = 1.4$ (b) $AR = 4.3$

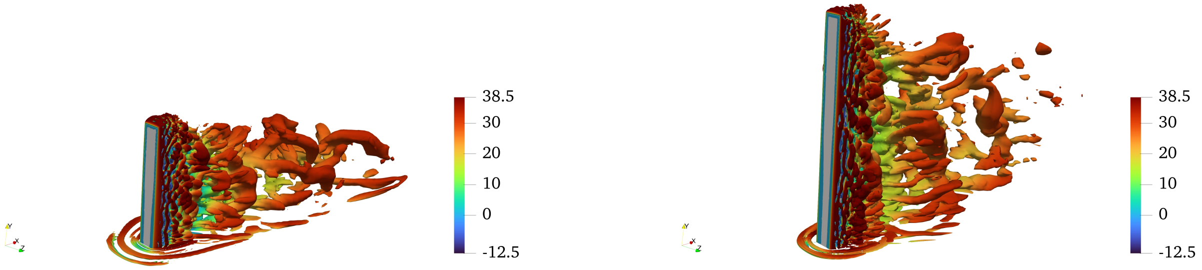

(c) $AR = 7.1$ (d) $AR = 12.9$

FIG. 7. Isosurface of the instantaneous flow structures at $Q_n = 0.1$, coloured by the mean streamwise velocity.

Fig. 8 illustrates the mean vorticity (ω_z) in the $z = 0$ plane for aspect ratios 1.4, 4.3, 7.1 and 12.9. Again, the results for an aspect ratio of 10 are not shown because they are similar to those for $AR = 12.9$. The mean vorticity

ω_z in Fig. 8(a) for $AR = 1.4$ is dominated by the downwash flow from the top of the cylinder, which evolves to a hairpin shape for larger aspect ratios. The lower part of the downwash flow for the aspect ratio of 4.3 shown in Fig. 8(b) extends to the ground, whereas it is above the ground for the larger aspect ratios as shown in Figs 8(c) and 8(d). Consequently, vortices from the junction of the cylinder with the wall and along the spanwise direction are allowed to develop, rotating in the opposite direction relative to the downwash flow from the cylinder top.

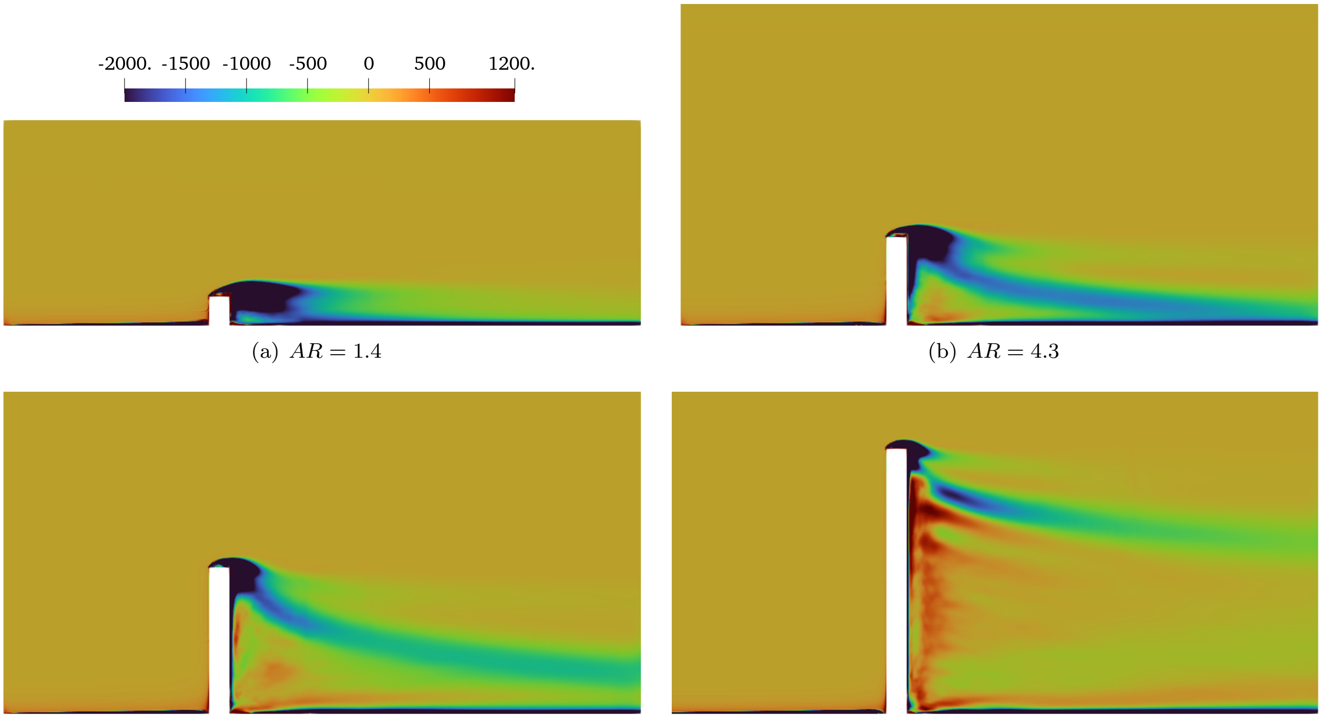

(a) $AR = 1.4$ (b) $AR = 4.3$

(c) $AR = 7.1$ (d) $AR = 12.9$

FIG. 8. Mean vorticity of ω_z on the $z = 0$ plane.

Contours of the mean pressure coefficient $C_p = (p - p_\infty)/(0.5\rho U_\infty^2)$ together with the mean streamlines on the $z = 0$ plane are displayed in Fig. 9. The thick white lines in Fig. 9 denote the locations of zero streamwise velocity, which are instructive in determining flow behaviour such as the separation, reattachment and also the recirculation length in the wake. The incoming flow impinges upon the frontal surfaces of the cylinder, causing positive pressure regions on the upstream side, while the flow separates from the leading edges of the free ends, forming negative pressure areas downstream. The aspect ratio mainly influences the distribution and magnitude of the pressure in the wake. As indicated by the white line and the streamlines in Fig. 9, the separated flow from the top may be restricted by the ground close by, forming the recirculating bubble R in the wake of the cylinders with aspect ratios of 1.4 and 4.3 shown in Fig. 9(a) and Fig. 9(b). In the bubble R, the separated flow goes back towards the trailing edge of the top surface. As the reflected flow refills the separated region, the pressure will increase, although it is still negative. As the aspect ratio increases, the effect of the ground on the separated flow from the top is weakened. As a consequence, no evident bubbles are found near the separated flow for larger aspect ratios, as shown in Figs 9(c) and 9(d). In addition, due to the larger height allowing the flow development along the spanwise direction, the recirculation length in the wake of the cylinder with aspect ratio 12.9 in Fig. 9(d) is much smaller than that for the others, as implied by the thick white lines.

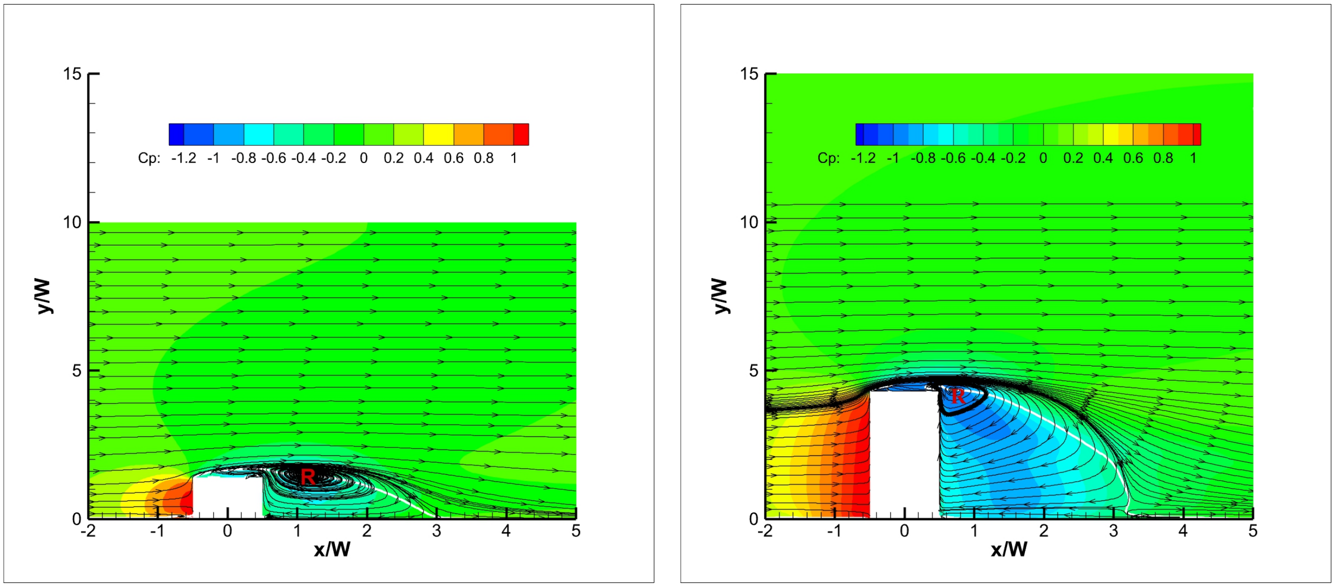

(a) $AR = 1.4$ (b) $AR = 4.3$

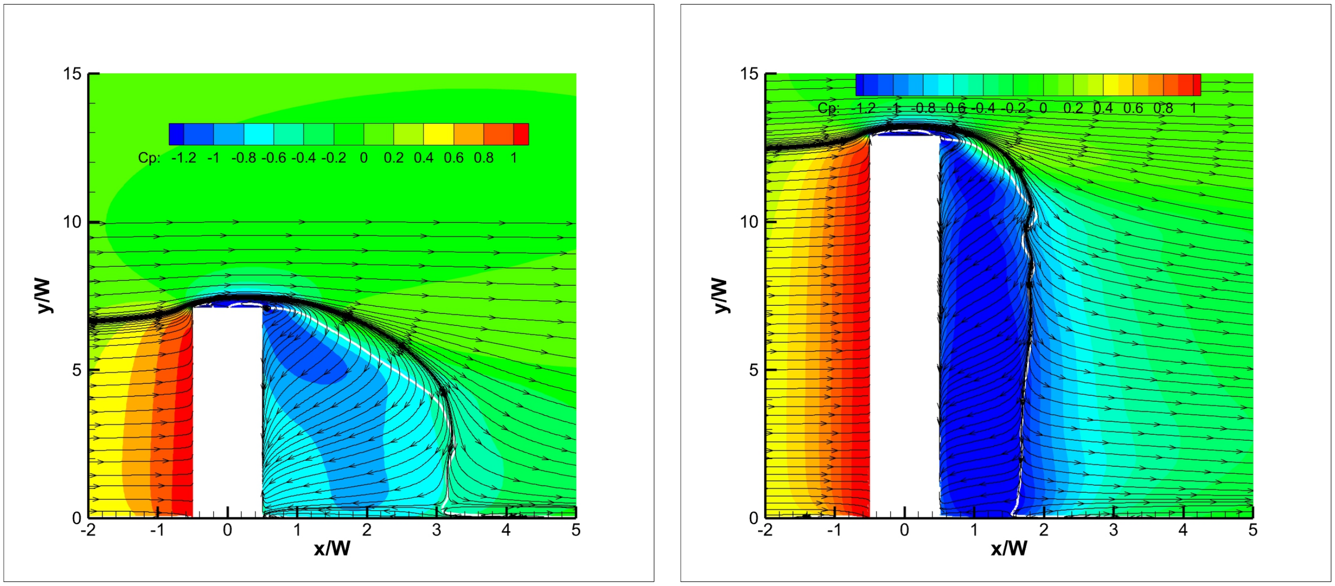

(c) $AR = 7.1$ (d) $AR = 12.9$

FIG. 9. Flow patterns around the cylinders in the $z = 0$ plane.

C. Near-wall flow topologies of the FWMCs

Flow interactions near the free end and the wall junction of the cylinder are mainly responsible for the different aerodynamic characteristics compared to square cylinders with infinite length. Studies on the near-wall flow topologies are instructive for a greater understanding of flow evolutions around FWMCs and pressure distributions on the walls, giving insight into the noise generation mechanisms. To visualise the effect of the aspect ratio on the near-wall flow topology close to the cylinder ends, Fig. 10 shows mean streamlines on planes 0.5 mm ($0.07W$) from the surfaces near the free ends of the cylinders. To visualise the flow around the free ends better and facilitate comparisons, only the top part with a length equal to W is shown in Fig. 10, coloured by the mean streamwise velocity. Critical points, including the focus (labelled with a red circle), saddle (diamond) and node (triangle) points, are identified in Fig. 10. Definitions of these critical points can be found in [49]. As illustrated, the near-wall flow topology surrounding the free ends changes significantly with increase of the aspect ratio, especially for the top surface. No evident critical points are found from the near-wall flow patterns for aspect ratio 1.4 as shown in Fig. 10(a), indicating fully separated flows from the leading edges. The near-wall flow topology depicted in Fig. 10(c) for aspect ratio 7.1 seems to be the most complicated. Apart from the four foci and two saddles on the top surface, two additional foci can be recognized on the rear surface, which are the trace of the connector strand developed in the wake of the cylinder, as reported by Porteous et al.[14]. With the aspect ratio increased to 12.9, two foci and one saddle are formed on the top surface along with two foci on the rear surface, as shown in Fig. 10(d). In addition, another focus is observed on the lateral surface, implying the upper part of the 'tornado' shaped vorticity as described by Martinuzzi and Tropea[50].

Fig. 11 shows details of the flow patterns on planes 0.5 mm above the free ends. Critical points, including the saddle, focus and node are identified from the in-plane mean streamlines, together with contours of the mean pressure coefficient. The dashed red lines labelled (S) indicate lines of separation nodes, which mean the streamlines cross the line going inwards. The blue dashed lines (R) are attachment nodes, formed by outward streamlines. Details about the separation nodes and the attachment nodes can be found in Fig. 5 of [8]. In addition, the thick white lines indicate locations with zero mean streamwise velocity, and all the critical points lie on these lines, consistent with their definitions. The red solid rectangle indicates the location of the cylinder. Since the square FWMCs have salient edges, the incoming flow separates from each edge. As indicated by Figs 7 and 8, with the increase of the aspect ratio, the flow separation becomes more coherent along the spanwise direction. Therefore, Fig. 11 demonstrates the evolution of the interaction between the separated flow from the side and the top surfaces. In general, as the aspect ratio increases, the separated flow moves closer to the top surface and the region enclosed by the white solid lines,

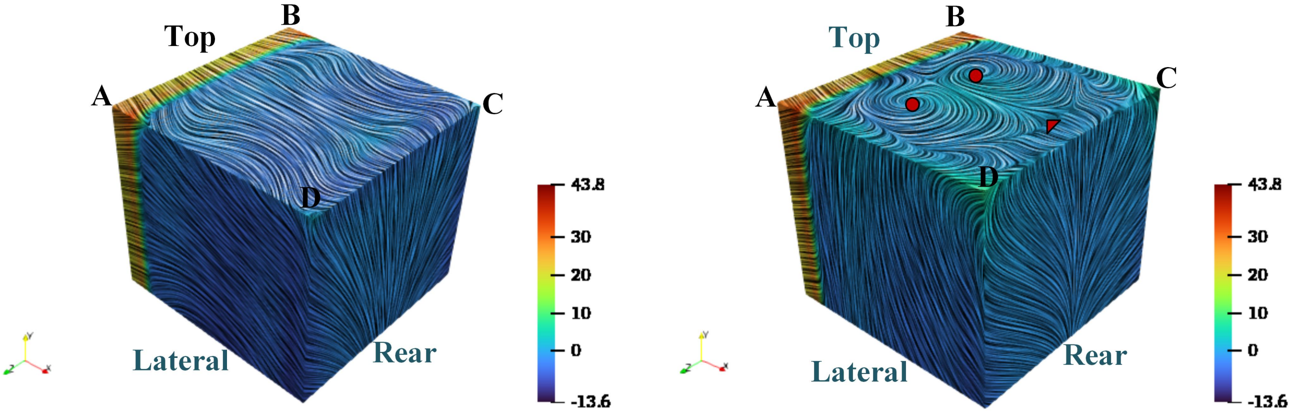

(a) $AR = 1.4$ (b) $AR = 4.3$

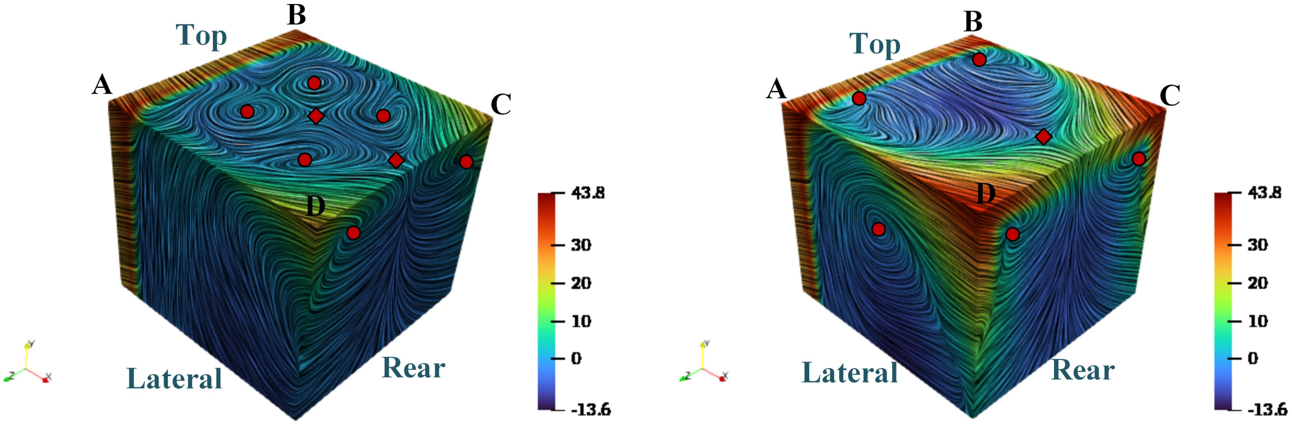

(c) $AR = 7.1$ (d) $AR = 12.9$

FIG. 10. Flow topology on planes 0.5 mm offset from the surfaces near the free ends, coloured by the mean streamwise velocity (circle: focus, diamond: saddle and triangle: node).

within which flow reverses, is shrunk.

According to the previous study[44], high levels of pressure fluctuations (P_{rms}) acting on the cylinder surfaces always occur in regions close to the edges connecting the lateral and rear surfaces. The near-wall flow topologies 0.5 mm away from the lateral surface on the $z = 4$ mm plane and away from the rear surface on the $x = 4$ mm plane, are shown in Fig. 12 and Fig. 13 respectively. Contours of the fluctuating pressure are also shown, expressed in decibels ($P_{ref} = 2 \times 10^{-5}$ Pa). In Fig. 12, projections of the lateral surfaces of the cylinders are depicted by the white rectangle labelled as 'ABCD'. Two foci $F1$ and $F2$ can be observed on the $z = 4$ mm plane alongside the lateral surface for aspect ratio 1.4 in Fig. 12(a). These two foci are imprints of the tornado vortex formed beside the cylinder and the recirculation region developed in the wake, respectively. When the aspect ratio is increased to 4.3, these foci disappear while a node $N1$ arises, causing high levels of pressure fluctuation in the wake, as shown in Fig. 12(b). Instead of one notable node, an attachment node line ($N1$) is found for aspect ratios of 7.1 and 12.9, as can be seen in Fig.

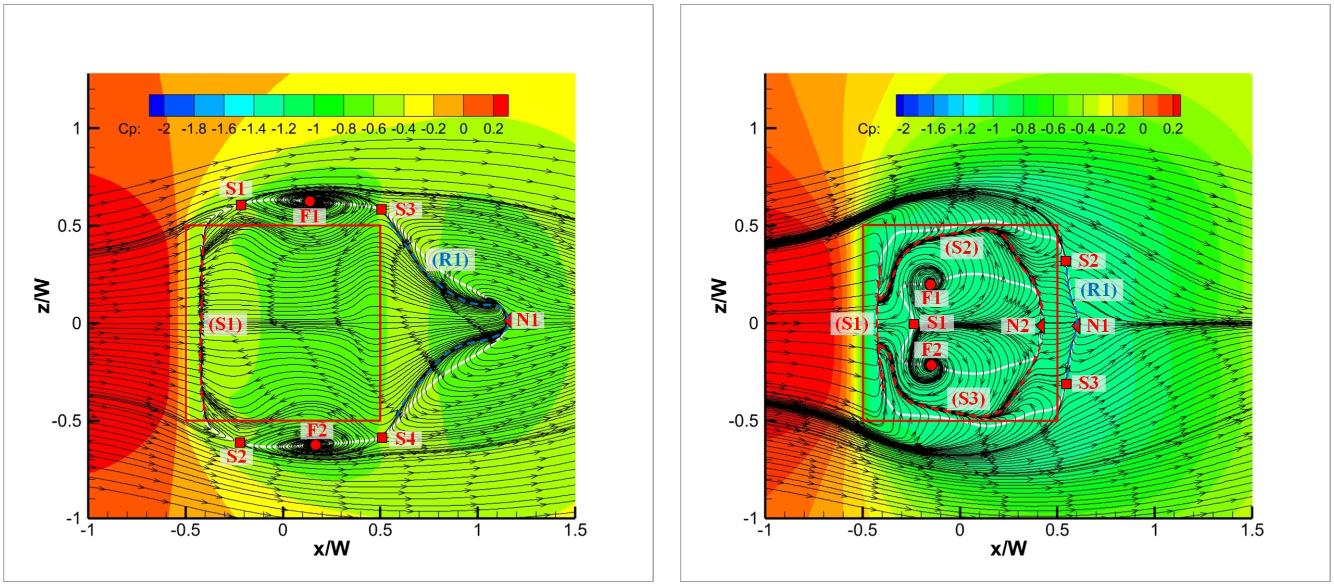

(a) $AR = 1.4$ (b) $AR = 4.3$

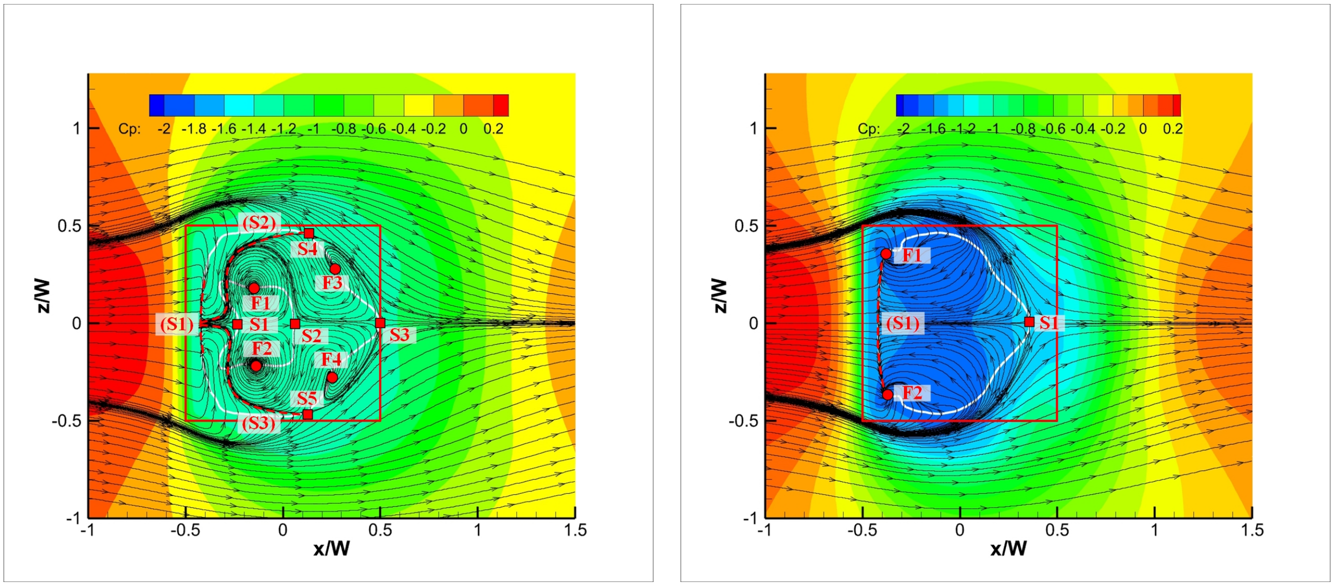

(c) $AR = 7.1$ (d) $AR = 12.9$

FIG. 11. Flow topology on planes 0.5 mm offset from the top surface of the FWMCs, coloured by the mean pressure coefficient (circle: focus, diamond: saddle and triangle: node).

12(c) and Fig. 12(d). As the aspect ratio is increased, the attachment node line ($N1$) moves closer to the cylinder while the pressure fluctuations grow, affecting the pressure distributions on the lateral surfaces of these cylinders. In summary, the pressure fluctuations acting on the lateral surfaces are mainly affected by the flow development in the wake as described above. In particular, another focus $F1$ can be seen in Fig. 12(d) near the free top of the cylinder with $AR = 12.9$, implying a new flow regime is developed around the tip. In Fig. 13, the position of the rear surface is indicated as 'ABEF', while the edge 'AB' is the same as that in the lateral surface in Fig. 12. The pressure levels inside the largest region 'ABEF' in Fig. 13(d) are highest with more coherent streamlines, due to the development of the vortex shedding in the wake.

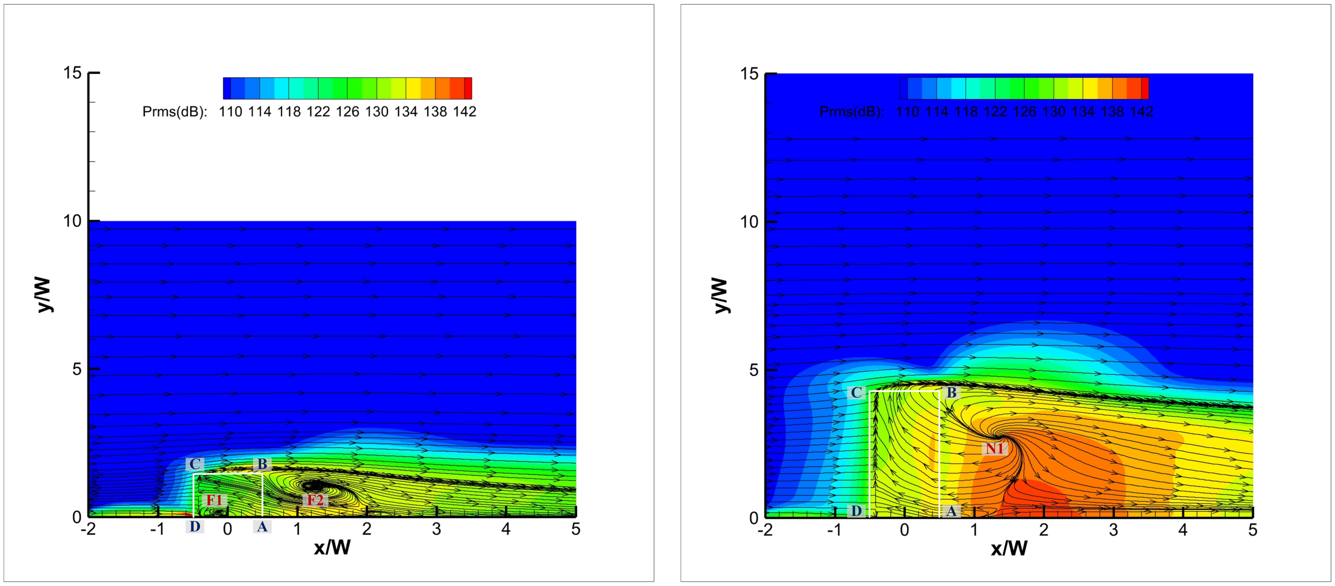

(a) $AR = 1.4$ (b) $AR = 4.3$

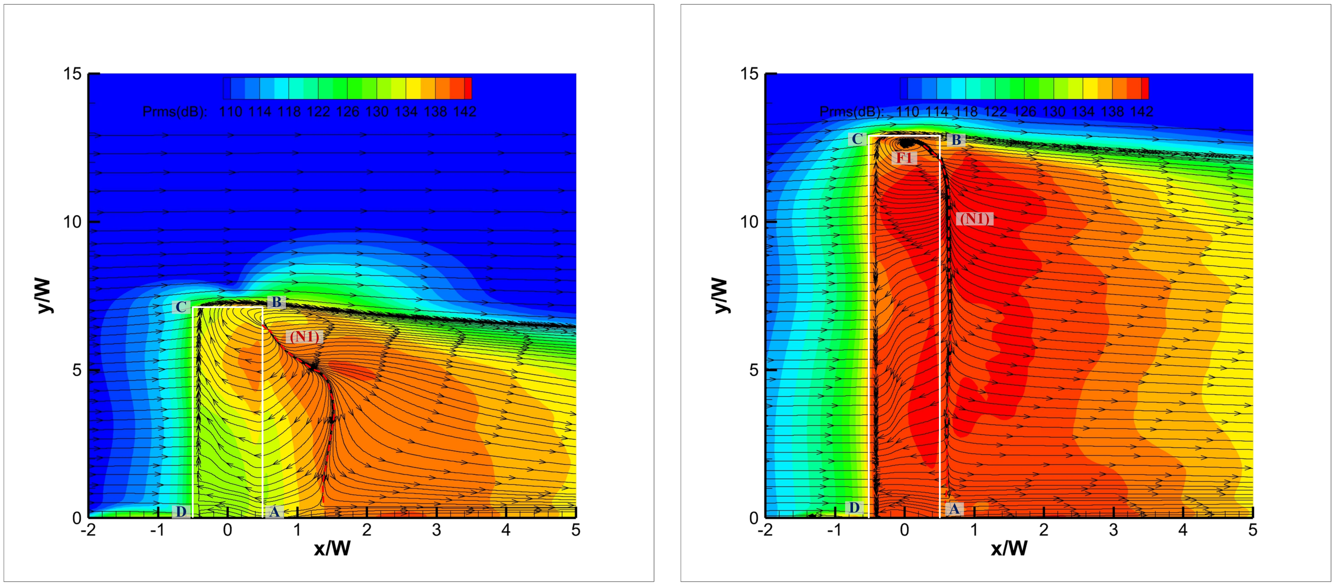

(c) $AR = 7.1$ (d) $AR = 12.9$

FIG. 12. The near-wall flow topology together with contours of P_{rms} on the $z = 4$ mm plane.

Fig. 14 shows the flow patterns 0.5 mm above the ground, surrounding the wall-mounting junction. Although the main features of the flow patterns are quite similar, with two foci and a recirculation region formed in the wake, a horseshoe vortex is only found at this height passing alongside the cylinder with aspect ratio 1.4, as shown in Fig. 14(a). The horseshoe vortex is an indicator of the three-dimensional flow, which is suppressed as the aspect ratio is

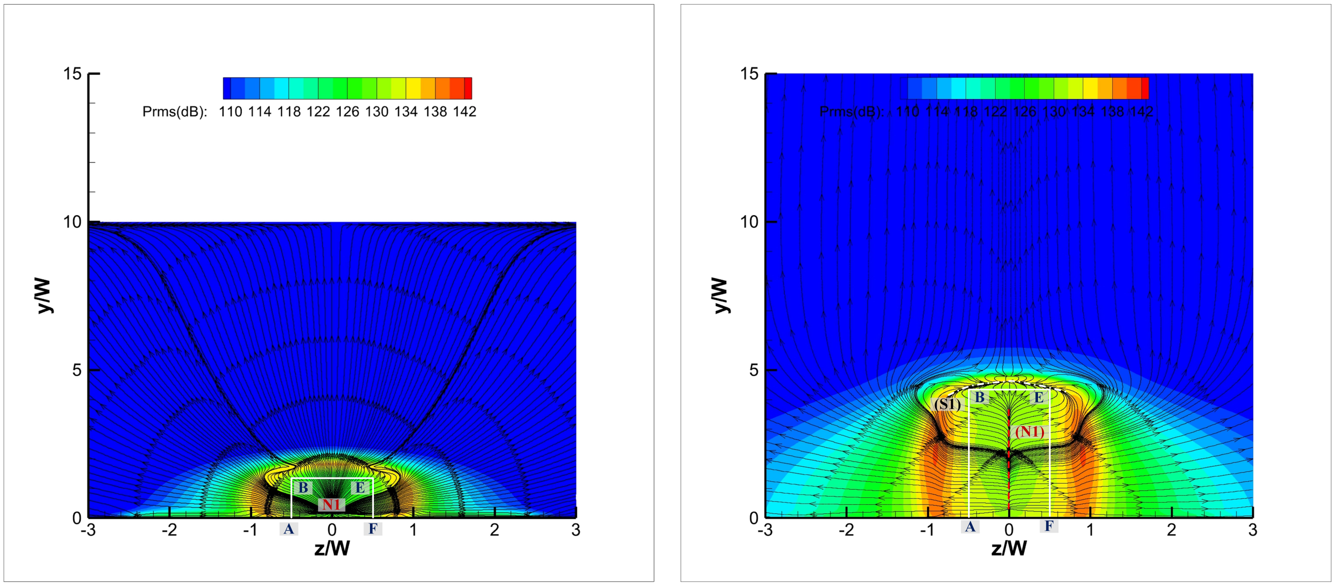

(a) $AR = 1.4$ (b) $AR = 4.3$

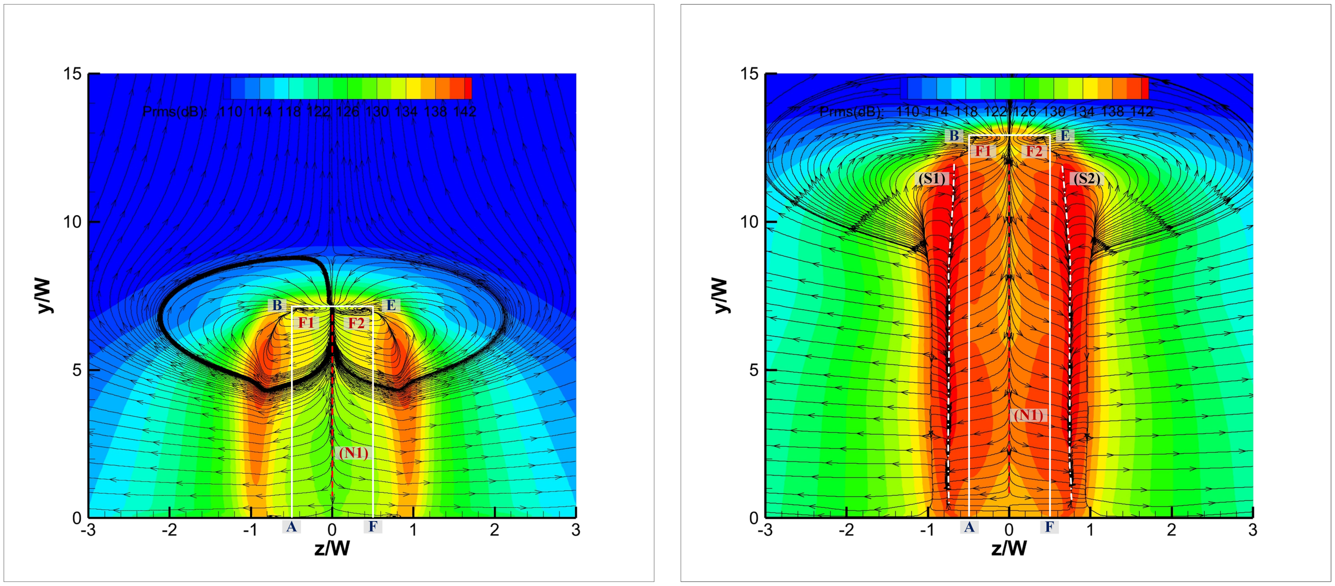

(c) $AR = 7.1$ (d) $AR = 12.9$

FIG. 13. The near-wall flow topology together with the fluctuating pressure on the $x = 4$ mm plane.

increased. The most evident difference illustrated in Fig. 14 is the recirculation length in the wake denoted by L_{rec}. The recirculation length can be determined based on the thick white lines indicating locations with zero streamwise velocity. According to Fig. 8, for sufficiently large aspect ratios, coherent vortices are developed along the spanwise direction between the wall-mounting junction and the free end, such as shown in Fig. 8(d). As a consequence, the separated flow at the free end cannot interact directly with the fluid along the ground, leading to a much shorter recirculation length near the ground around the junction.

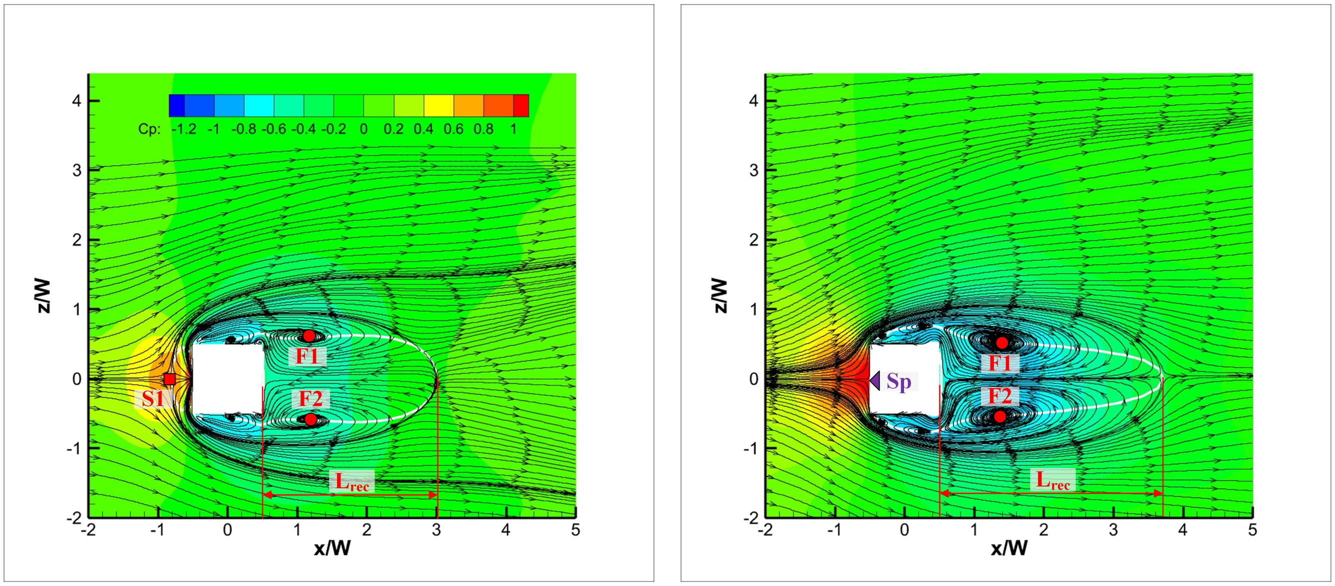

(a) $AR = 1.4$ (b) $AR = 4.3$

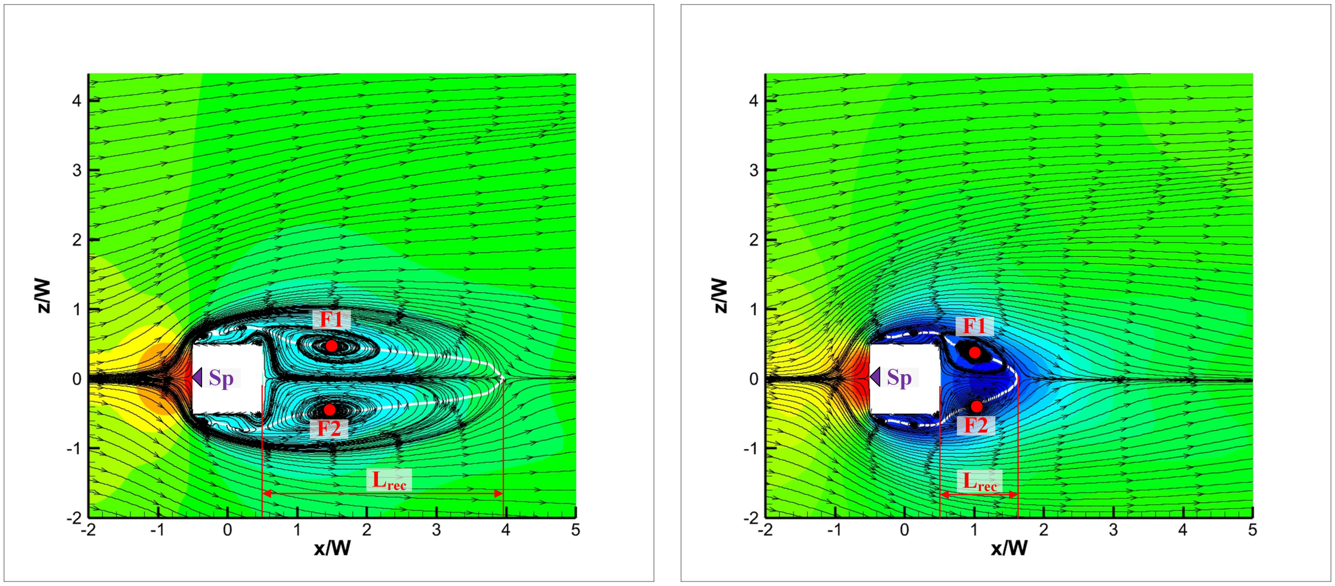

(c) $AR = 7.1$ (d) $AR = 12.9$

FIG. 14. Flow patterns around the junction of the cylinders on the $y = 0.5$ mm plane.

D. Pressure distributions on the cylinders

Distributions of the surface pressure are important in describing the flow features and are responsible for the dipole noise sources emitting sound to the far field. Fig. 15 displays the mean pressure coefficients C_p along the cylinder surfaces on the $x = 0$ plane and the $z = 0$ plane respectively. For the purpose of comparison and validation, the pressure coefficients along a wall-mounted cube ($AR = 1$) are also shown as the dashed lines in Fig. 15, which are plotted based on the authors' previous work[42]. The pressure profiles shown in Fig. 15 start from the ground and the distances are normalised by the length of the indicated surface. Therefore, the abscissa representing the position in Fig. 15 ranges from 0 to 3 for all the cases.

Fig. 15(a) shows the pressure distributions along the cylinder surface on the spanwise plane through the middle of the cylinder ($x = 0$). These are symmetric and the pressure coefficients are negative as they are all in the separated region. In general, the pressure coefficients on the $x = 0$ plane reduce (larger negative values) as the aspect ratio increases. However, it is interesting that the pressure coefficients C_p at the starting point, which is on the mounting wall, are nearly identical for the cylinders with aspect ratios of 1.4, 4.3 and 7.1, while the pressure coefficients on the top surface are quite different. In contrast, the results for $AR = 10$ and 12.9 differ at their starting points but are almost overlapping on the top surface. This indicates that the flow patterns induced by the square FWMCs studied in this paper fall into two different categories, which is also implied by the PSDs of the aerodynamic coefficients shown in Fig. 6. Considering the pressure distributions on the $z = 0$ plane shown in Fig. 15(b), the values of C_p on the front surface are close to 1, caused by the impingement of the incoming flow. The overall trends of the pressure distributions with varying aspect ratio in Fig. 15(b) are similar to those observed in Fig. 15(a). The considerable change in C_p near the trailing edge (at position 2) on the top surface for aspect ratios of 10 and 12.9 is caused by the flow reattachment close to the trailing edge, as depicted in Fig. 9(d).

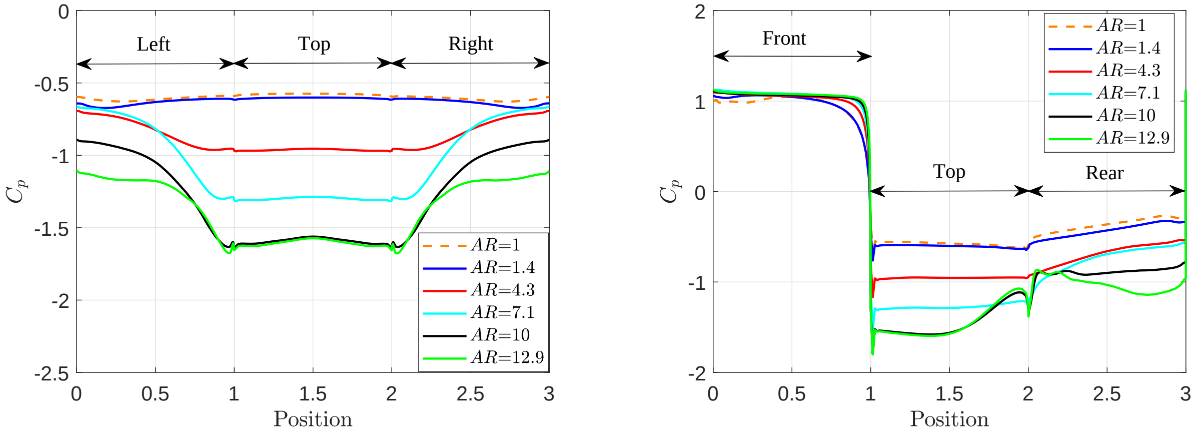

(a) $x = 0$ plane

(b) $z = 0$ plane

FIG. 15. Distributions of the mean pressure coefficient along the cylinder surfaces.

As discussed in Section II B, the pressure rate of change $\mathrm{d}p/\mathrm{d}t$ on the solid walls has a positive correlation with the equivalent dipole noise sources emitted to the far field. The fluctuating pressure acting on the cylinder surfaces are sampled every fifty time steps, namely, with a time interval of 5×10^{-5} s. Fig. 16 shows contours of $\mathrm{d}p/\mathrm{d}t$ acting on the cylinder surfaces, calculated based on Eq. 5. The distribution of $\mathrm{d}p/\mathrm{d}t$ for $AR = 10$ is omitted due to its similarity to that for $AR = 12.9$. The fluctuating pressure on the cylinder surfaces is collected over a sampling time of about 1 s, and the pressure rate of change is obtained using the central difference method with a second order accuracy. The PSD of the $\mathrm{d}p/\mathrm{d}t$ signal on every grid point is computed based on Welch's method with a Hanning window, giving a frequency resolution of about 10 Hz ($St = 0.002$). Contours shown in Fig. 16 are obtained by integrating each PSD up to 10 kHz, which is also the maximum frequency determined by the Shannon sampling theorem. Due to the direct impingement of the incoming flow, the pressure fluctuations on the frontal surfaces are negligible compared with those on the other surfaces and are therefore not shown. The pressure contour depicted on the left surface is the same as that for the right, considering the symmetry of the cylinders, and is labelled as the lateral surface in Fig. 16. As can be seen, distributions of the pressure rate of change $\mathrm{d}p/\mathrm{d}t$ on the cylinder surfaces are quite dependent on the aspect ratio. High levels of $\mathrm{d}p/\mathrm{d}t$ always occur in regions close to the edge connecting the lateral and rear surfaces, although the strength grows quickly as the aspect ratio is increased.

VI. EFFECT OF THE ASPECT RATIO ON THE RADIATED NOISE

A. Far-field noise prediction

At low Mach numbers, as considered here, the flow-induced noise emitted from a rigid body is mainly contributed by the dipole sources, associated with the pressure fluctuations acting on the solid surfaces. The noise propagating to the far field is predicted using the FW-H acoustic analogy in the commercial software FLUENT. The fluctuating pressure acting on the cylinder surfaces is sampled from the CFD simulations, and used as the input to the FW-H equation (Eq. (1)). Since the noise from these FWMCs is the focus of this work, the noise from the ground is not considered. Fig. 17 shows the spectra of the predicted noise at receivers 10 m ($1428W$) away from the origin (cylinder wall-mounting centre) along the streamwise, spanwise and the cross-flow directions. These noise spectra are computed using Welch's method similarly to that described for the aerodynamic coefficients. The frequency resolution is about 12 Hz, corresponding to a Strouhal number of 0.003. The noise emitted from the shortest cylinder is much lower than the others in the streamwise direction, as can be seen in Fig. 17(a), despite a pronounced peak at a Strouhal number around 0.235. In contrast, no evident peaks can be found in the noise spectra for the cylinders with $AR = 4.3$ and 7.1, while two small peaks around $St = 0.19$ and 0.24 appear for the aspect ratios of 10 and 12.9. The noise levels observed in the spanwise direction, shown in Fig. 17(b), are generally lower, apart from $AR = 1.4$. The noise levels in the cross-flow direction, shown in Fig. 17(c), are the highest, especially for the cylinders with large aspect

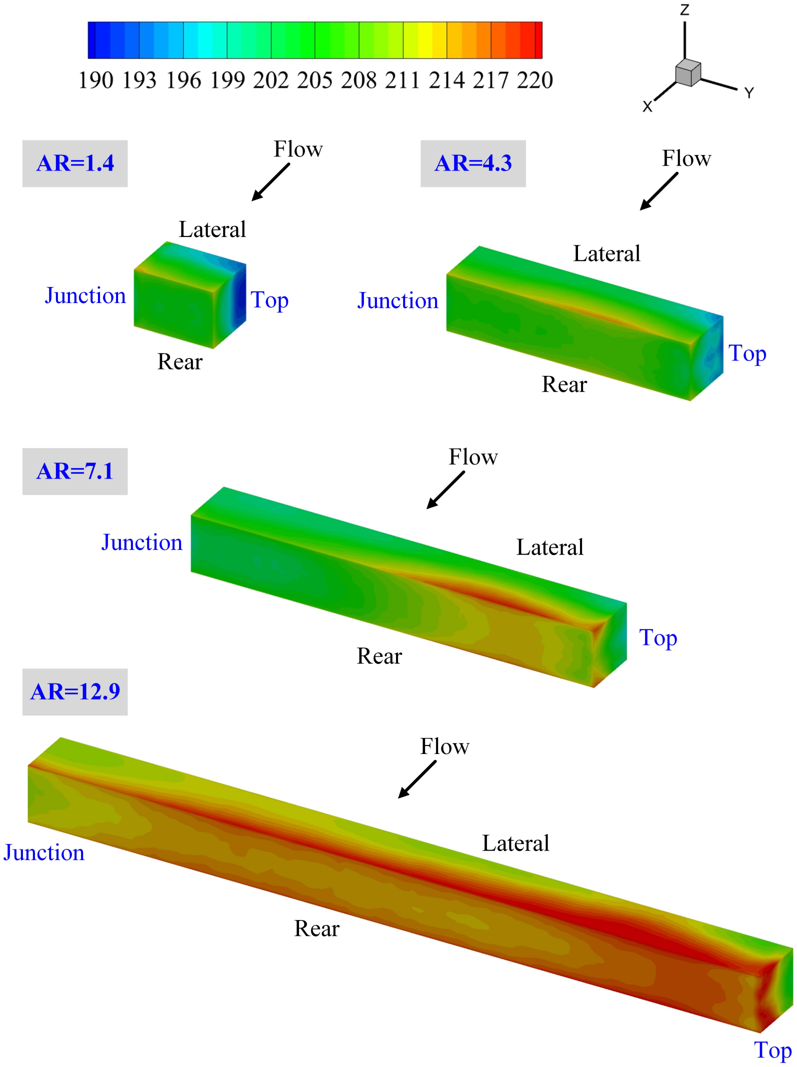

FIG. 16. Contours of the pressure rate of change (dp/dt) on the cylinder surfaces.

ratios. The noise spectra for $AR = 1.4$, 4.3 and 7.1 have a similar shape, with a strong tonal peak around $St = 0.1$. However, for the cylinders with larger aspect ratios, there are two tonal peaks at Strouhal numbers of 0.095 and 0.12; for comparison, an infinite square cylinder has a peak at $St \approx 0.13$.[51,52] For each cylinder, the frequencies of these tonal peaks in Fig. 17(c) are coincident with those shown in Fig. 6(c) for the side force coefficient.

The Overall Sound Pressure Levels (OASPL) at the three receivers are illustrated in Fig. 18, calculated by integrating the PSD spectra shown in Fig. 17 up to 9143 Hz ($St = 2$). Since the mean square acoustic pressure generated from solid boundaries is proportional to the area of the object[35], the area of sampled surfaces for cylinders with different aspect ratios needs to be normalised. For the purpose of comparison, the predicted noise for each case is normalised corresponding to the overall surface area of the shortest cylinder, namely $6.6W^2$. Therefore, the correction applied to

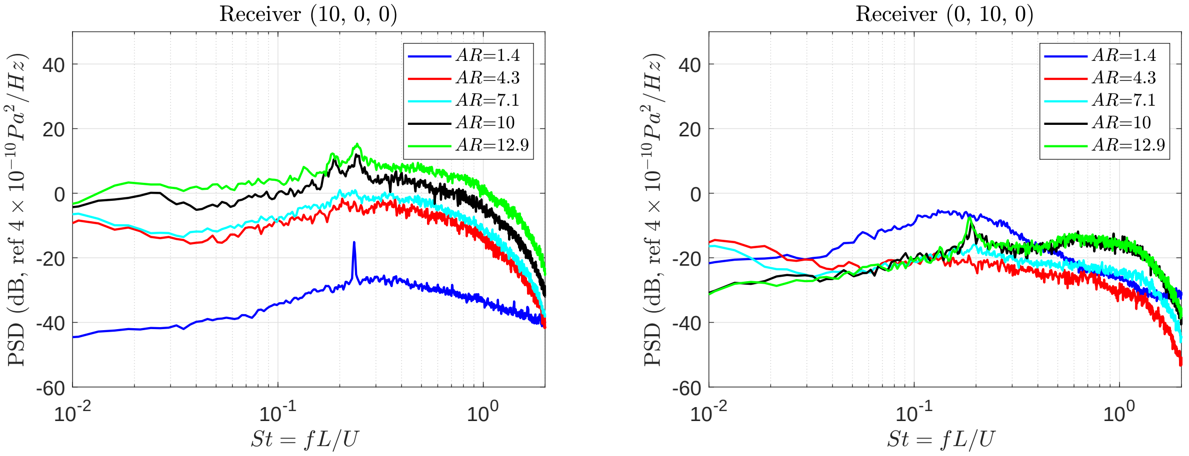

(a) Receiver in streamwise direction, (10 0 0)

(b) Receiver in spanwise direction, (0 10 0)

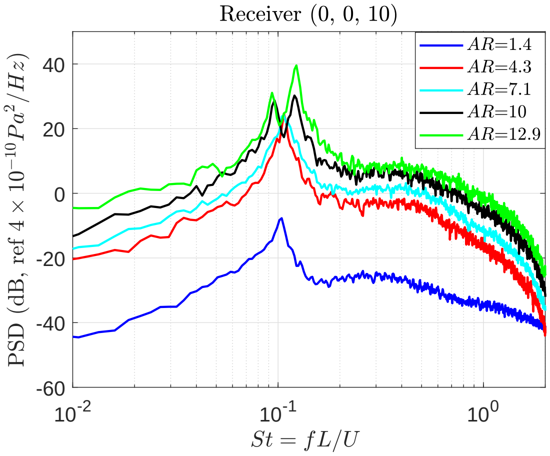

(c) Receiver in cross-flow direction, (0 0 10)

FIG. 17. PSDs of the predicted noise emitted from the FWMCs.

the noise is:

$$\begin{aligned} L_{cor} &= -10\log_{10}((WL + 2WH + 2HL)/6.6W^2) \\ &= -10\log_{10}((10 + 40AR)/66) \end{aligned} \tag{10}$$

as depicted in Fig. 18(a). Trends of the OASPL at the three receivers with varying aspect ratio are shown in Fig. 18(b). The radiated noise received at (10, 0, 0) in the streamwise direction and at (0, 0, 10) in the cross-flow direction grows quickly with the increase of the aspect ratio, even though the predicted noise is reduced due to the surface area correction shown in Fig. 18(a). In addition, the sound propagating in the cross-flow direction is always greater than that in the streamwise direction, the largest difference being about 12 dB for the longest cylinder. However, for the cylinder with $AR = 1.4$, the noise in the spanwise direction at (0, 10, 0) is much higher than that from the others. It drops dramatically by about 15 dB when the aspect ratio is increased to 4.3, while it then grows gradually with the further increase of the aspect ratio.

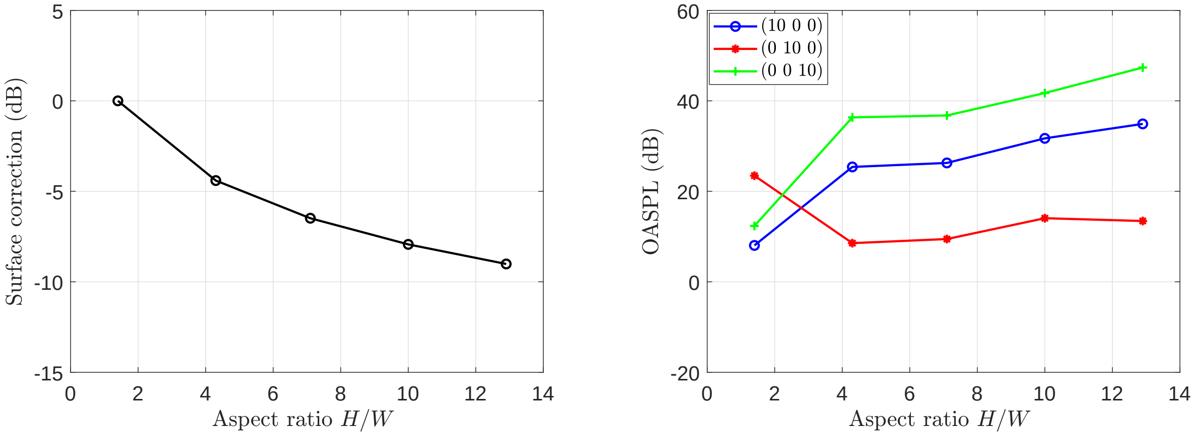

(a) Surface correction (b) OASPL

FIG. 18. OASPLs at different receivers for the FWMCs.

B. Mechanism of the tonal noise

As discussed above, tonal noise is observed at different receivers and changes with the aspect ratio, which is closely related with the underlying flow patterns. DMD described in Sec. II C is a technique that is helpful in studying complex flow processes. In particular, this method can extract frequency-specific modal information, making it suitable for tonal noise analysis. To explore the mechanism of the tonal noise emitted from these FWMCs, PSDs of dp/dt on the cylinder surfaces are integrated in narrow frequency bands containing the tones, illustrating the noise source distribution for the tonal noise of interest. The frequency range is determined as that in which the noise is greater than -10 dB relative to the tones. In addition, the DMD method is also applied to display the flow structure at the tonal frequency. To implement the DMD, 4000 instantaneous snapshots of the velocity field on the $z = 0$ plane are sampled for each cylinder with a time interval of 1×10^{-4} s. Fig. 19 shows the distribution of eigenvalues and spectrum of the DMD modes for the modal decomposition of $AR = 12.9$ as an example. The imaginary part and real part of the eigenvalues λ represent the frequency and growth/decay rate of the DMD modes, respectively. The amplitudes of the DMD modes are represented by b on a log scale. As shown in Fig. 19(a), despite a small number of outliers, the eigenvalues are tightly clustered around a unit circle in the Ritz space, indicating nearly zero growth/decay rates of the statistically stationary velocity data. The frequencies of the primary modes identified by DMD, as highlighted by the two red small circles in Fig. 19(b), coincide well with those observed from the tonal noise at the receiver (0 0 10) for the $AR = 12.9$.

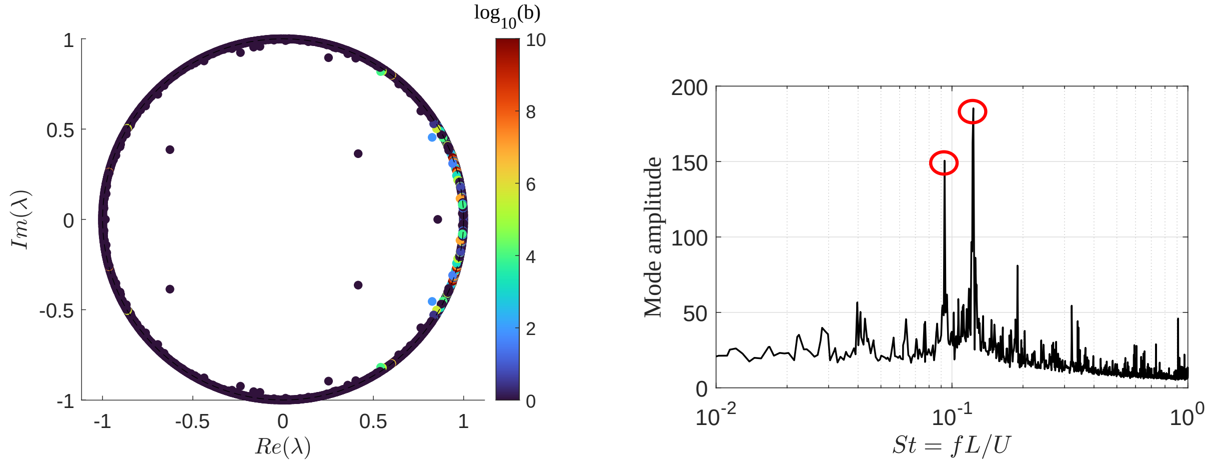

(a) Distribution of eigenvalues (b) Spectrum of DMD modes

FIG. 19. Eigenvalues and modes of DMD for $AR = 12.9$ as an example.

Figs 20 and 21 illustrate contours of the pressure rate of change $\mathrm{d}p/\mathrm{d}t$ and the streamwise vorticity ω_x computed based on the DMD, relating to the tonal noise observed at the cross-flow receiver (0 0 10) for the $AR = 7.1$ and $AR = 12.9$, respectively. The grey rectangles in the vorticity plots represent the cylinder positions. The distribution of noise sources matches well with the flow patterns. It turns out the dominant noise received at (0 0 10) for FWMCs with $AR \leq 7.1$ is mainly due to the periodic flow shedding from the free end. As the cylinder is lengthened further, a secondary tone emerges related with the coherent flow pattern formed near the junction. Fig. 22 presents results related with the prominent peak at $St = 0.235$ received at the downstream position (10 0 0) for $AR = 1.4$, shown in Fig. 17(a). It is interesting to identify that this tonal noise from the shortest cylinder is related with the upstream horseshoe vortex. Imprints of the horseshoe vortex can also be seen from the noise sources in Fig. 22(a). Flow interactions between the horseshoe vortex and the separated flow from the leading edges lead to the high levels of $\mathrm{d}p/\mathrm{d}t$ shown in Fig. 22(a), affecting the noise emitted to the far field. Due to the gradual decay of the horseshoe vortex with increasing aspect ratio, no more evident peaks appear along this direction for longer cylinders. However, although this tonal noise along the streamwise direction is related to the horseshoe vortex formed upstream, it does not mean it is the dominant component of the overall noise emitted to the receiver (10 0 0), because the frequency band of this tone is very narrow, as shown in Fig. 17(a).

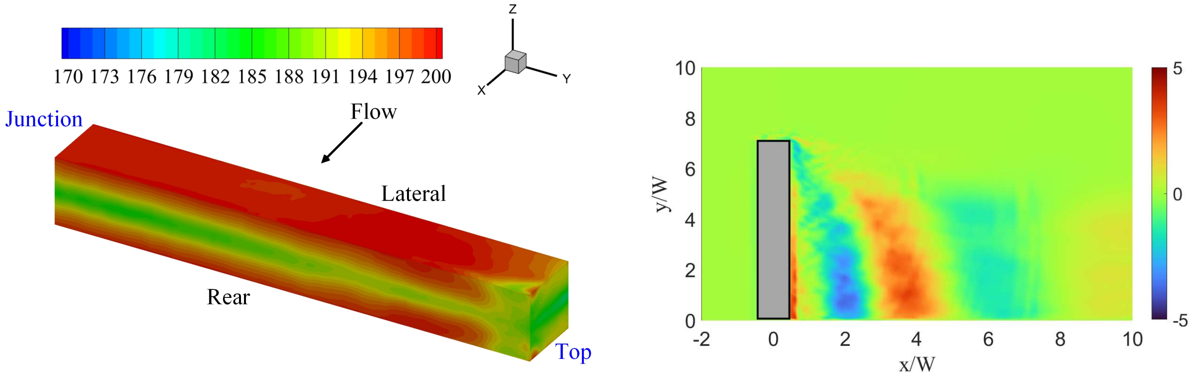

(a) Contour of $\mathrm{d}p/\mathrm{d}t$ integrated from $St = 0.085$ to 0.13 (b) The vorticity ω_x at $St = 0.1$ on the $z = 0$ plane

FIG. 20. Contour of $\mathrm{d}p/\mathrm{d}t$ and the vorticity computed based on DMD, relating to the tonal noise observed at the receiver (0 0 10) for $AR = 7.1$.

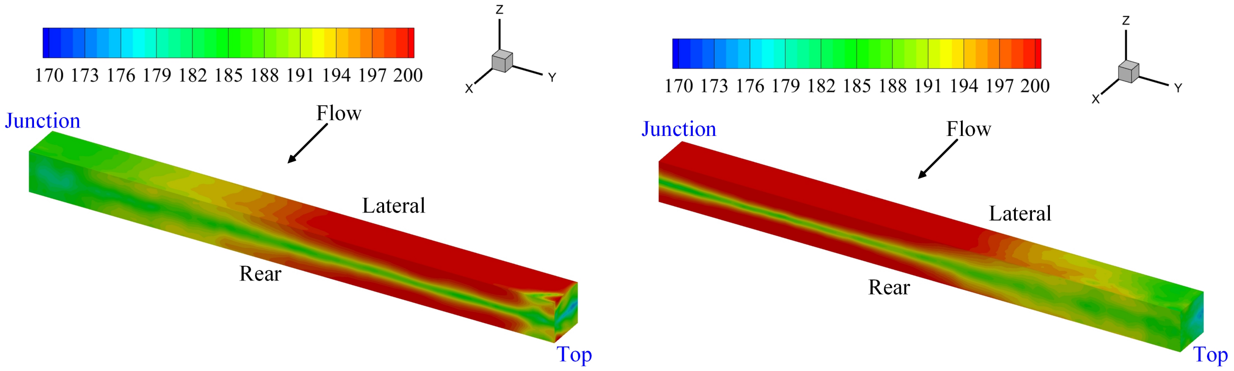

(a) Contour of $\mathrm{d}p/\mathrm{d}t$ integrated from $St = 0.088$ to 0.1 (b) Contour of $\mathrm{d}p/\mathrm{d}t$ integrated from $St = 0.112$ to 0.13

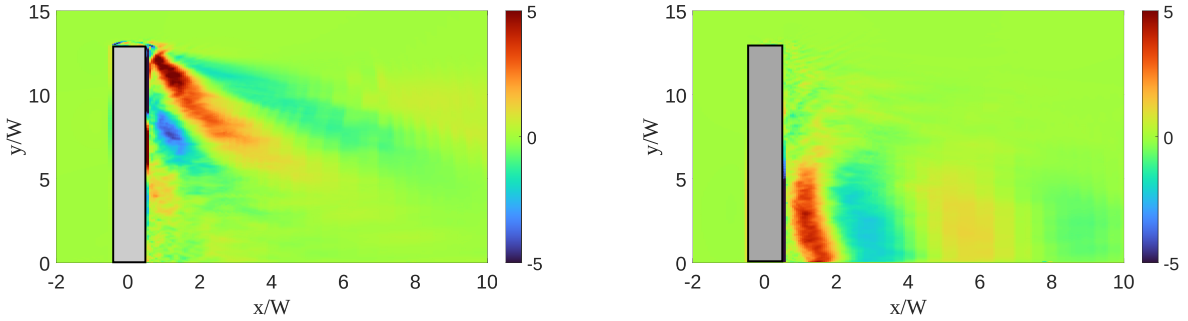

(c) The vorticity ω_x at $St = 0.095$ on the $z = 0$ plane (d) The vorticity ω_x at $St = 0.12$ on the $z = 0$ plane

FIG. 21. Contours of $\mathrm{d}p/\mathrm{d}t$ and the vorticities computed based on DMD, relating to the tonal noise observed at the receiver (0 0 10) for $AR = 12.9$.

VII. CONCLUSIONS

Flow features relevant to the noise from finite wall-mounted square cylinders with different aspect ratios are studied numerically and the mechanism of tonal noise emitting to the far field is investigated. The flow is at a Reynolds number of 1.5×10^4, which lies in the range where the flow over a square cylinder is independent of Reynolds number.

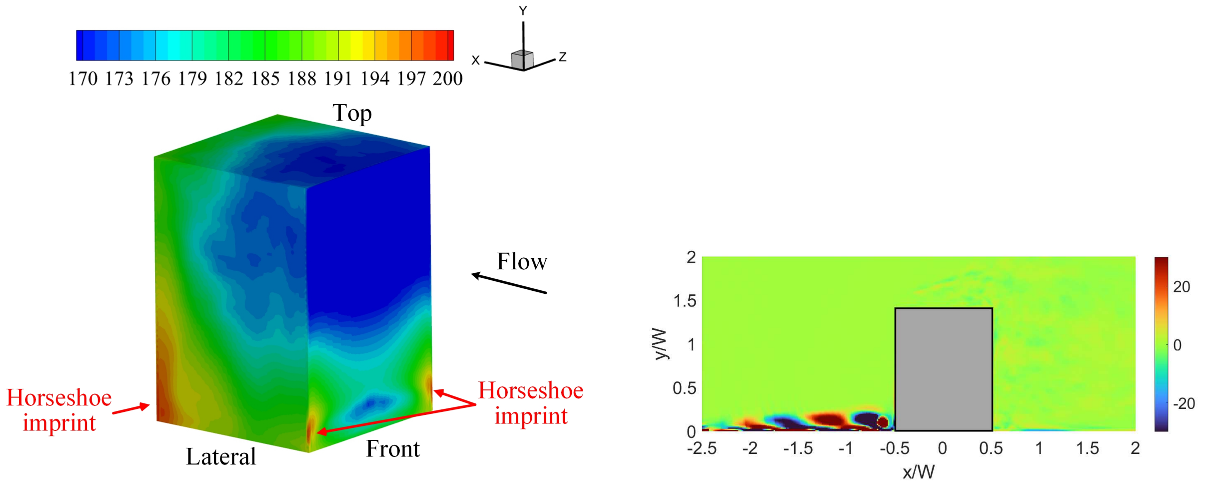

(a) Contour of dp/dt integrated from $St = 0.23$ to 0.24

(b) The vorticity ω_z at $St = 0.235$ on the $z = 0$ plane

FIG. 22. Contour of dp/dt and the vorticity computed based on DMD, relating to the tonal noise observed at the receiver (10 0 0) for $AR = 1.4$.

Five aspect ratios ranging from 1.4 to 12.9 are considered. The flow behaviours are examined using the DDES model, while the radiated noise is predicted using the FW-H acoustic analogy based on the sampled surface pressures.

Distinct peaks are found in the PSDs of C_s for all the studied cylinders; however, both the number and the shape of these peaks are affected by the aspect ratio. The horseshoe vortices become less significant as the aspect ratio is increased. The wake for $AR = 1.4$ is dominated by the downwash flow from the free end; however, as the aspect ratio increases, the flow structures in the wake along the spanwise direction become more and more coherent due to the development of the vortex shedding. The near-wall flow topologies of the top surface are most sensitive to the variation of the aspect ratio. In addition, high levels of the pressure rate of change dp/dt on the cylinder surfaces appear near the edge connecting the lateral and rear surfaces, which are positively correlated with the dipole noise sources.

In general, the far-field noise is most prominent in the cross-flow direction and the radiated noise grows as the aspect ratio increases, even taking into account the surface area correction. A single pronounced tonal peak centred at $St = 0.1$ is observed in the noise spectra in the cross-flow direction for $AR = 1.4$, 4.3 and 7.1, while two peaks at $St = 0.095$ and 0.12 are found for the aspect ratios of 10 and 12.9. Both the noise source distribution and the underlying flow pattern related to these tonal peaks are examined to explore the mechanism of tonal noise. It is found that the distribution of noise sources matches well with the extracted flow modes. The flow shedding from the free ends is most responsible for the tonal noise in the cross-flow direction for the cylinders not longer than $7.1W$. As the aspect ratio is further increased, coherent flow structures developed near the wall-mounting junction will cause a secondary tone. The prominent peak observed in the noise spectrum at the streamwise receiver (10 0 0) for the shortest cylinder is closely related with the horseshoe vortex formed upstream.

ACKNOWLEDGMENTS

This research is supported by China Postdoctoral Science Foundation (No.2021M702595) and Natural Science Foundation of China (No.52305127). The simulations in this paper were carried out on the iridis 5 supercomputer at the University of Southampton.

[1] H. Wang and Y. Zhou, “The finite-length square cylinder near wake,” Journal of Fluid Mechanics **638**, 453–490 (2009).

[2] H. Jang, C. Ozdemir, J.-H. Liang, and M. Tyagi, “Oscillatory flow around a vertical wall-mounted cylinder: Dynamic mode decomposition,” Physics of Fluids **33**, 025113 (2021).

[3] Z. Hu, H. Liu, N. Chen, J. Hu, and F. Tong, “Vortex shedding noise and flow mode analysis of cylinder with full/partial porous coating,” Aerospace Science and Technology **106**, 106154 (2020).

[4] Z. Li, T. Tang, Y. Liu, E. J. Arcondoulis, and Y. Yang, “Numerical study of aerodynamic and aeroacoustic characteristics of flow over porous coated cylinders: Effects of porous properties,” Aerospace Science and Technology **105**, 106042 (2020).

[5] M. Zhao, A.-A. Mamoon, and H. Wu, “Numerical study of the flow past two wall-mounted finite-length square cylinders in tandem arrangement,” Physics of Fluids **33**, 093603 (2021).

[6] R. Porteous, D. J. Moreau, and C. J. Doolan, “A review of flow-induced noise from finite wall-mounted cylinders,” Journal of Fluids and Structures **51**, 240–254 (2014).

[7] Y. Yauwenas, R. Porteous, D. J. Moreau, and C. J. Doolan, “The effect of aspect ratio on the wake structure of finite wall-mounted square cylinders,” Journal of Fluid Mechanics **875**, 929–960 (2019).

[8] Y. Cao, T. Tamura, D. Zhou, Y. Bao, and Z. Han, “Topological description of near-wall flows around a surface-mounted square cylinder at high reynolds numbers,” Journal of Fluid Mechanics **933**, A39 (2022).

[9] G. Chen, X.-B. Li, B. Sun, and X.-F. Liang, “Effect of incoming boundary layer thickness on the flow dynamics of a square finite wall-mounted cylinder,” Physics of Fluids **34**, 015105 (2022).

[10] S. Behera and A. K. Saha, “Characteristics of the flow past a wall-mounted finite-length square cylinder at low reynolds number with varying boundary layer thickness,” Journal of Fluids Engineering **141** (2019).

[11] S. Shinde, K. Maki, and E. Johnsen, “Spatially evolving turbulent boundary-layer flow over a wall-mounted cube,” AIAA Journal **60**, 1565–1577 (2022).

[12] M. Rastan, H. Shahbazi, A. Sohankar, M. M. Alam, and Y. Zhou, “The wake of a wall-mounted rectangular cylinder: Cross-sectional aspect ratio effect,” Journal of Wind Engineering and Industrial Aerodynamics **213**, 104615 (2021).

[13] D. J. Moreau and C. J. Doolan, “Flow-induced sound of wall-mounted finite length cylinders,” AIAA journal **51**, 2493–2502 (2013).

[14] R. Porteous, D. J. Moreau, and C. J. Doolan, “The aeroacoustics of finite wall-mounted square cylinders,” Journal of Fluid Mechanics **832**, 287–328 (2017).

[15] S. Becker, C. Hahn, M. Kaltenbacher, and R. Lerch, "Flow-induced sound of wall-mounted cylinders with different geometries," AIAA journal **46**, 2265–2281 (2008).

[16] T. F. Geyer, "Vortex shedding noise from finite, wall-mounted, circular cylinders modified with porous material," AIAA Journal **58**, 2014–2028 (2020).

[17] P. J. Schmid, "Dynamic mode decomposition of numerical and experimental data," Journal of Fluid Mechanics **656**, 5–28 (2010).

[18] M. O. Burak, B. Gustafsson, B. Malla, and E. J. Gutmark, "Screech noise characterization using dynamic mode decomposition and shadowgraph imagery," in *22nd AIAA/CEAS Aeroacoustics Conference* (2016) p. 2797.

[19] C. Prasad and D. V. Gaitonde, "A time-domain linear method for jet noise prediction and control trend analysis," Aerospace Science and Technology **121**, 107377 (2022).

[20] A. Broatch, M. Carreres, J. García-Tíscar, and M. Rodríguez-Pastor, "Numerical analysis of combustion noise in an atmospheric swirl-stabilized LDI burner through modal decomposition techniques," Aerospace Science and Technology **137**, 108281 (2023).

[21] A. Broatch, R. Navarro, J. García-Tíscar, and F. Ramírez, "Evaluation of different FW-H surfaces and modal decomposition techniques for the acoustic analysis of UAV propellers through detached eddy simulations," Aerospace Science and Technology , 108956 (2024).

[22] C. Yang, J. Zhang, and Z. Huang, "Numerical study on cavitation–vortex–noise correlation mechanism and dynamic mode decomposition of a hydrofoil," Physics of Fluids **34** (2022).

[23] C. W. Knisely, "Strouhal numbers of rectangular cylinders at incidence: a review and new data," Journal of fluids and structures **4**, 371–393 (1990).

[24] D. K. Kaushik, D. E. Keyes, and B. F. Smith, "Newton-Krylov-Schwarz methods for aerodynamics problems: compressible and incompressible flows on unstructured grids." Tech. Rep. (Argonne National Lab., IL (US), 1999).

[25] P. R. Spalart and S. R. Allmaras, "A one equation turbulence model for aerodynamic flows," AIAA Journal **94**, 439 (1992).

[26] P. Spalart, W. Jou, M. Strelets, S. Allmaras, *et al.*, "Comments on the feasibility of LES for wings, and on a hybrid RANS/LES approach," Advances in DNS/LES **1**, 4–8 (1997).

[27] H. K. Versteeg and W. Malalasekera, *An introduction to computational fluid dynamics: the finite volume method* (Pearson education, 2007).

[28] S. R. Allmaras and F. T. Johnson, "Modifications and clarifications for the implementation of the spalart-allmaras turbulence model," in *Seventh international conference on computational fluid dynamics (ICCFD7)* (2012) pp. 1–11.

[29] J. Fröhlich and D. von Terzi, "Hybrid LES/RANS methods for the simulation of turbulent flows," Progress in Aerospace Sciences **44**, 349–377 (2008).

[30] F. Menter and M. Kuntz, "Adaptation of eddy-viscosity turbulence models to unsteady separated flow behind vehicles," in *The Aerodynamics of Heavy Vehicles: Trucks, Buses, and Trains* (Springer, 2004) pp. 339–352.

[31] P. R. Spalart, S. Deck, M. Shur, K. Squires, M. K. Strelets, and A. Travin, "A new version of detached-eddy simulation, resistant to ambiguous grid densities," Theoretical and Computational Fluid Dynamics **20**, 181–195 (2006).

[32] J. E. Ffowcs Williams and D. L. Hawkings, "Sound generation by turbulence and surfaces in arbitrary motion," Philosophical Transactions of the Royal Society of London. Series A, Mathematical and Physical Sciences **264**, 321–342 (1969).

[33] S. Glegg and W. Devenport, *Aeroacoustics of low Mach number flows: fundamentals, analysis, and measurement* (Academic Press,

2017).

[34] Y. Khalighi, A. Mani, F. Ham, and P. Moin, "Prediction of sound generated by complex flows at low mach numbers," AIAA journal **48**, 306–316 (2010).

[35] N. Curle, "The influence of solid boundaries upon aerodynamic sound," Proceedings of the Royal Society. London. Series A. Mathematical, Physical and Engineering Sciences **231**, 505–514 (1955).

[36] K. Taira, S. L. Brunton, S. T. M. Dawson, C. W. Rowley, T. Colonius, B. J. Mckeon, O. T. Schmidt, S. Gordeyev, V. Theofilis, and L. S. Ukeiley, "Modal analysis of fluid flows: an overview," AIAA Journal **55**, 4013–4041 (2017).

[37] C. W. Rowley, I. Mezić, S. Bagheri, P. Schlatter, and D. S. Henningson, "Spectral analysis of nonlinear flows," Journal of Fluid Mechanics **641**, 115 (2009).

[38] K. K. Chen, J. H. Tu, and C. W. Rowley, "Variants of dynamic mode decomposition: boundary condition, Koopman, and Fourier analyses," Journal of Nonlinear Science **22**, 887–915 (2012).

[39] J. N. Kutz, S. L. Brunton, B. W. Brunton, and J. L. Proctor, *Dynamic mode decomposition: data-driven modeling of complex systems* (Dynamic Mode Decomposition: Data-Driven Modeling of Complex Systems, 2016).

[40] C. W. Rowley and S. T. M. Dawson, "Model reduction for flow analysis and control," Annual Review of Fluid Mechanics **49**, 387–417 (2017).

[41] J. H. Tu, C. W. Rowley, D. M. Luchtenburg, S. L. Brunton, and J. N. Kutz, "On dynamic mode decomposition: theory and applications," Journal of Computational Dynamics **1**, 391–421 (2014).

[42] Y. Wang, D. Thompson, and Z. Hu, "Effect of wall proximity on the flow over a cube and the implications for the noise emitted," Physics of Fluids **31**, 077101 (2019).

[43] Y. Wang, Z. Hu, and D. Thompson, "Numerical investigations on the flow over cubes with rounded corners and the noise emitted," Computers & Fluids **202**, 104521 (2020).

[44] Y. Wang, D. Thompson, and Z. Hu, "Numerical investigations on the flow over cuboids with different aspect ratios and the emitted noise," Physics of Fluids **32**, 025103 (2020).

[45] I. Castro and A. Robins, "The flow around a surface-mounted cube in uniform and turbulent streams," Journal of fluid Mechanics **79**, 307–335 (1977).

[46] S. Depardon, J. Lasserre, J. Boueilh, L. Brizzi, and J. Borée, "Skin friction pattern analysis using near-wall PIV," Experiments in Fluids **39**, 805–818 (2005).

[47] E. Achenbach, "Experiments on the flow past spheres at very high reynolds numbers," Journal of Fluid Mechanics **54**, 565–75 (1972).

[48] V. Kolář, "Vortex identification: New requirements and limitations," International journal of heat and fluid flow **28**, 638–652 (2007).

[49] J. M. Délery, "Robert legendre and henri werlé: toward the elucidation of three-dimensional separation," Annual review of fluid mechanics **33**, 129–154 (2001).

[50] R. Martinuzzi and C. Tropea, "The flow around surface-mounted prismatic obstacles placed in a fully developed channel flow," J Fluids Eng **115**, 85–92 (1993).

[51] X. Liu, J. Zhang, D. Thompson, E. Latorre Iglesias, G. Squicciarini, Z. Hu, M. Toward, and D. Lurcock, "Aerodynamic noise of high-speed train pantographs: comparisons between field measurements and an updated component-based prediction model," Applied

Acoustics **175**, 107791 (2021).

[52]E. Latorre Iglesias, D. Thompson, J. M. Paniagua, and J. G. García, “On the feasibility of a component-based approach to predict aerodynamic noise from high-speed train bogies,” Applied Acoustics **211**, 109536 (2023).